Applied Catalysis B: Environmental 205 (2017) 238–253

Contents lists available at ScienceDirect

Applied Catalysis B: Environmental

journal homepage: www.elsevier.com/locate/apcatb

Low temperature steam reforming of methane: A combined isotopic and microkinetic study

P.N. Kechagiopoulos[a,*], S.D. Angeli[b], A.A. Lemonidou[b]

[a] Chemical and Materials Engineering Group, School of Engineering, University of Aberdeen, Aberdeen, AB24 3UE, UK
[b] Laboratory of Petrochemical Technology, Department of Chemical Engineering, Aristotle University of Thessaloniki, GR-54124 Thessaloniki, Greece

ARTICLE INFO

Article history:
Received 3 October 2016
Received in revised form 5 December 2016
Accepted 10 December 2016
Available online 12 December 2016

Keywords:
Methane steam reforming
Microkinetic model
Kinetic isotope effect
Nickel
Rhodium

ABSTRACT

Low temperature steam reforming in combination with hydrogen selective membranes presents great potential of intensifying the classical industrial hydrogen production process via natural gas. This concept can lead to significant environmental and process benefits, such as reduced energy needs, milder material stability requirements and considerably simplified process layouts via e.g. avoiding the use of downstream WGS reactors. Ni and Rh based catalysts supported on La_2O_3-CeO_2-ZrO_2, already identified as active and stable at these conditions, are further investigated in the current work aiming at the elucidation of reaction kinetics. Temperature programmed experiments of methane conversion in steam reforming and decomposition modes in conjunction with isotopic investigations using CD_4 are carried out, showing that cleavage of a C—H bond participates in the rate determine step, whereas steam derived intermediates do not. A thermodynamically consistent microkinetic model considering a comprehensive set of surface pathways is also developed. The model describes correctly experimental trends, predicting surface CH_3 dehydrogenation to be rate limiting. Estimated model parameters further help elucidate the different catalysts' activities. The combined approach presented shows potential to accelerate catalyst and process design efforts for the promising low temperature steam reforming hydrogen production process.

© 2016 Elsevier B.V. All rights reserved.

1. Introduction

Hydrogen presents significant potential as an energy carrier that can drive the implementation of efficient and environmentally benign energy systems. Industrial hydrogen production via natural gas steam reforming is accompanied, though, by significant CO_x emissions from the burner supplying heat to the endothermic reaction. The need for intensification of the process has spurred the search for alternative concepts, with methane steam reforming (MSR) at a low temperature range of 400–550 °C being one such promising approach. The milder operating conditions lead to lower operation and materials costs, while the favorable temperature eliminates the need for separate water gas shift reactors. Thermodynamic limitations, resulting in low CH_4 conversions and H_2 yields, can be surpassed using selective membranes that remove hydrogen *in situ*. As a result, hydrogen is separated with high purity and at the same time the reforming reaction equilibrium is shifted to the product side [1,2].

The use of highly active and coke resistant catalysts at these low temperatures is a key factor to the success of such a system. Ni-based catalysts combine good activity and low cost [3,4], whereas noble metal ones, although typically of higher activity than Ni, are limited by their high cost [5]. The support type can also contribute to the properties of an ideal reforming catalyst [3]. Reducible supports such as CeO_2 and CeO_2–ZrO_2 mixed oxides are good candidates for low temperature MSR due to their active role in the redox mechanism through the mobility of surface oxygen species [6–13]. Addition of La [14] can further improve the oxygen storage capacity of CeO_2–ZrO_2, enhancing both the coke resistance [15,16], and thermal stability of the catalyst [17].

A series of Ni and Rh catalysts supported on lanthana and/or ceria modified zirconia were prepared and evaluated for their performance in low temperature steam reforming [18,19], showing high activity at the 400–550 °C region and close to equilibrium CH_4 conversion at relatively short contact times. The notably stable behavior of both metals supported on lanthana doped ceria-zirconia during model biogas steam reforming at ambient pressure highlighted the importance of CeO_2 in the support. The Ni-based catalyst, especially, performed remarkably at extended high pressure 90-h-stability tests of model biogas steam reforming, showing

* Corresponding author.
E-mail address: p.kechagiopoulos@abdn.ac.uk (P.N. Kechagiopoulos).

http://dx.doi.org/10.1016/j.apcatb.2016.12.033
0926-3373/© 2016 Elsevier B.V. All rights reserved.

minimal amount of carbon formation (0.05 wt%). The low coking tendency and resistance to sintering effects over both metals were ascribed to the active oxygen species provided by ceria and the thermal stabilization effect and low coking affinity of lanthana. TPO and TPH analysis of the carbonaceous deposits showed that the dominating type of carbon is highly reactive and can be easily removed by oxidation or hydrogenation at 500–550 °C. Analysis of these deposits at different reaction times showed a stable carbon amount with time on stream, implying that at least part of it is an active reaction intermediate.

As recently reviewed [6], the kinetics of MSR have been the subject of numerous studies. Wei and Iglesia [20–25] concluded to a comprehensive mechanistic picture for CH_4 activation in the presence or absence of any co-reactant (CO_2, H_2O) on Ni- and various noble metal-based catalysts. Identical forward CH_4 reaction rates, rate constants, kinetic isotope effects, and activation energies were measured, with CH_4 rates found to be limited solely by C—H bond activation and unaffected by the identity or concentration of co-reactants. Nørskov and coworkers [26], combining first-principles calculations and experimental investigations on pure transition metals, determined a CH_4 dissociation and a CO formation step to be kinetically limiting, with the latter dominating at lower temperatures. Vlachos et al. have notably developed an elaborate microkinetic model, based on semi-empirical and first principle techniques [27,28], able to describe CH_4 steam and dry reforming over Rh catalysts [29,30]. For both reactions, CH_4 activation was found to be rate-determining [29], in agreement with Wei and Iglesia [21]. Deutschmann et al. have presented a multi-step microkinetic model also describing both reforming reactions over Ni catalysts [31,32], however a sensitivity to oxidative dehydrogenation indicated the kinetic relevance of steam in MSR. Chen et al. [33,34] in their microkinetic model over Ni, interestingly, accounted also for filamentous carbon formation. Blaylock et al. initially developed a microkinetic model based on DFT-calculated Ni(111) thermochemical data [35] that was further extended via calculations on Ni(100) and Ni(211) surfaces to improve the description of data on multifaceted Ni catalysts [36]. The same approach for CH_4 dry reforming was recently considered in the work of Fan et al. [37].

In the current work a combination of temperature-programmed experimental techniques, isotopic studies and comprehensive microkinetic modelling is presented, aiming at obtaining insight on the kinetics of low temperature MSR over the promising La_2O_3-CeO_2-ZrO_2 supported Ni and Rh catalysts.

2. Procedures

2.1. Experimental

2.1.1. Catalyst preparation and characterization

The catalysts were prepared via the wet impregnation method using $Ni(NO_3)_2{\cdot}6H_2O$ (Merck) and $RhCl_3{\cdot}3H_2O$ (Pressure Chemical) as active metal precursors and lanthanum doped cerium – zirconium oxide (78 wt% ZrO_2, 17 wt% CeO_2, 5 wt% La_2O_3, Mel Chemicals) as catalyst support. In the following, the catalysts are referred to as M(x)CeZrLa, where M is the active metal and x the metal loading wt%. The surface area of the prepared materials was measured by N_2 adsorption at 77 K, using the multipoint BET analysis method (Autosorb-1 Quantachrome). X-ray diffraction (XRD) patterns were obtained using a Siemens D500 diffractometer, with Cu K_α radiation. The reducibility of the catalysts and the metal dispersion were investigated through temperature programmed reduction and desorption respectively. Further details on the experimental equipment, catalytic testing procedures and elaborate characterization have been reported elsewhere [19].

2.1.2. Catalyst testing and mechanistic experiments

The activity towards the conversion was tested at the temperature range of 400–550 °C at atmospheric pressure and methane partial pressure of 0.25–0.5 (H_2O/CH_4 ratio of 1–3). The data-set collected consisted of 54 experimental points. The laboratory unit is equipped with a mass flow-controlled system for gases admission, an UFLC pump (Shimadju) for the feeding of water to the reactor through a preheated line, a fixed bed quartz reactor, and an online gas chromatograph. Fresh catalyst powder was used in each test in order to avoid deactivation effects. In each test the GHSV was kept constant, while the temperature was decreased stepwise after equilibration of the system conditions [19]. The absence of external and internal mass transport limitations during the catalytic tests was ensured through the evaluation of criteria proposed by Mears [38] and Weisz-Prater [39], respectively.

In order to gain information on the main reaction pathways and explore the existence of Kinetic Isotope Effects (KIE), a series of temperature programmed experiments were performed in a gas flow system using a U-tube reactor. The catalyst sample (20 mg) was placed in the reactor and reduced for 1 h at 550 °C in 20% H_2/He. The temperature was then raised from ambient to 650 °C at a rate of 10 °C/min under the reaction mixture (50 mL/min). Tests with deuterated methane (CortecNet, 99% atom enrichment) were also conducted over the Ni and Rh catalysts. For all runs the reactor exit was monitored online with a quadrupole mass analyzer (Omnistar) by following the m/z signals: He: 4, H_2: 2, D_2: 4, CH_4: 16, CD_4: 20, CO: 28 and CO_2: 44. Overlapping fragments contributions on various gas compounds were taken into account. In order to avoid reoxidation of the reduced catalyst by the steam, the reaction mixture was in by-pass mode until the temperature of 350 °C for Ni-based catalyst and 250 °C for Rh-based catalyst. In temperature programmed methane decomposition experiments, the reaction mixture was 1.7% CH_4 (or CD_4) in He and Ar. For the steam reforming reaction, the reaction mixture consisted of 1.7% CH_4 (or CD_4) and 5.1% H_2O (S/C = 3) or 3.4% H_2O (S/C = 2) using as dilution gas He and Ar. To ensure that CD_4 concentrations measured are not affected by the formation of D_2O, contributing also at m/z = 20, CD_4 consumption rates were also calculated using the CD signal at m/z = 14 with the appropriate coefficient between masses at 20 and 14 accounted for. This ratio was calculated based on separate tests using a flow of pure CD_4 to the mass analyzer. Identical consumption rates were measured suggesting that exchange side reactions with H_2O and D species are not important under the experimental conditions applied. As above, standard criteria were applied to ensure measurements were conducted under explicit kinetic control and were unaffected by transport limitations, while multiple tests were carried out at the same conditions to verify the repeatability of results.

2.2. Modelling

2.2.1. Model formulation and computation details

The microkinetic model presented in this work has been developed with a FORTRAN-based (micro) kinetic modeling platform, the microkinetic engine (MKE), previously described in Metaxas et al. [40] and further used in Sprung et al. [41]. As experimental data have been collected under explicit kinetic control (see Ref. [19] and Section 2.1.2), a plug flow reactor model is used for the simulation of experiments. Furthermore, the pseudo-steady state approximation is made for the surface intermediates, accounting explicitly for the mass balance of the catalyst active sites. The DASPK 2.0 solver [42,43] is used for the solution of the above differential and algebraic equations system, while the Rosenbrock [44] and Levenberg–Marquardt [45,46] optimization methods are used for estimation of the model's parameters, namely chemisorption enthalpies and sticking coefficients. The latter can account for the

physical and chemical catalyst properties and are often referred to as catalyst descriptors [47].

The microkinetic model is thermodynamically consistent at both enthalpic and entropic level with surface reaction enthalpies and entropies being correlated to analogous gas-phase reactions. The entropies of surface species are calculated through the subtraction of the gaseous translational entropy from the equivalent gas species entropy, while surface species enthalpies are correlated to the equivalent gaseous ones through the respective species chemisorption enthalpies. Collision theory is used to calculate maximum values for adsorption pre-exponential factors, the latter corrected by a sticking coefficient. Adsorption steps are considered as non-activated, while activation energies of forward steps of all reactions among surface species are calculated using the UBI-QEP method [48,49]. The Supporting Information provides elaborate details on the kinetic model parametrization and the implementation of thermodynamic consistency.

2.2.2. Surface reaction network description

A previously developed microkinetic model, successfully applied to the evaluation of kinetic isotope effects observed over a $Ni/NiAl_2O_4$ catalyst [41], is substantially extended in this work. A comprehensive set of 78 elementary reaction steps among 5 molecules and 13 surface species is considered, accounting elaborately for multiple surface reaction pathways for reactants activation and products formation (Table 1). The catalytic network describes methane activation on the catalyst surface through dissociative adsorption (R1–2). Formed CH_3* species can further dehydrogenate up to the bare carbon atom through direct (R17-22) or oxidative pathways, the latter taking place either with O* (R23–28) or OH* (R29–34) species. CH_x* species can also couple with each other, as described in reactions (R35–40), which have been included in the model to investigate the importance of scrambling rates of such species [50]. The decomposition of carbon oxides has been accounted for in reactions (R57–68), while several steps involving the dissociation of CHO* and the COOH* species or their interaction with other surface species have been included in reactions (R41–56) and (R69-78), respectively. Water is assumed to adsorb molecularly (R3–4), followed by a stepwise dissociation to OH* (R5–6) and O* (R7–8) species, accompanied by H* formation, with the former OH* further possibly interacting with itself in R9–10. Carbon oxides are assumed to desorb molecularly (R13–16), while an associative desorption has been considered for hydrogen (R11–12).

3. Results

3.1. Catalyst characterization

Since the characterization and activity evaluation of the catalysts have been reported in previous work, only basic characterization results of the catalysts are presented here. The specific surface area and the metal dispersion of the catalysts are shown in Table 2 and the diffraction patterns are shown in Fig. S1 in the Supporting Information. The crystalline phase apparent in the support material is $Zr_{0.84}Ce_{0.16}O_2$. No peaks corresponding to single crystalline phase La_2O_3 are observed implying that it is finely dispersed or in an amorphous state. In the diffraction pattern of the Ni-based catalyst, the characteristic peaks of the support are present and those of NiO as well, indicating successful impregnation of the metal on the support. In the diffractogram of the Rh-based catalyst, no peaks for Rh_2O_3 were detected, mostly due to its low content. The temperature of maximum reduction of each catalyst as determined by temperature programmed reduction is also reported in Table 1. The reduction of both catalysts can be achieved at relatively mild conditions, important for the application of the low temperature steam reforming concept, with T_{max} at 180 °C and 480 °C for the Rh-based and the Ni-based catalyst respectively. A reduction peak of low intensity was also observed to the profile of the bare support, which was ascribed to the partial reduction of ceria.

3.2. Temperature programmed methane decomposition

Methane decomposition is one of the first steps of the steam reforming mechanism and is of high importance since it has been reported to be kinetically relevant [20,29]. The distribution of gases during the temperature programmed methane decomposition over Ni(10)CeZrLa is presented in Fig. 1a, while in Fig. 1b a detail of the gas distribution close to the initiation temperature is shown.

At the low temperature range, from ambient temperature to the temperature of 370 °C, the detected gas at the outlet of the reactor is only methane, as the decomposition reaction does not take place. Methane decomposition over Ni(10)CeZrLa starts at 370 °C, at which temperature a sharp consumption peak of methane is observed. The consumption of methane is accompanied by the production of CO_2 followed by CO, H_2O and H_2 (Fig. 1b). Catalytic methane decomposition reaction leads to the production of solid C and gaseous H_2 as follows:

$$CH_4\,(g) \rightarrow C\,(s) + 2H_2\,(g) \quad (1)$$

Since no oxidant is present in the gaseous phase, the evolution of oxygen-containing gases can only be realized by the participation of the lattice oxygen from the support. As a result, CO_2 and H_2O are probably produced via the following reaction:

$$CH_4\,(g) + 4O\,(s) \rightarrow CO_2\,(g) + 2H_2O\,(g) \quad (2)$$

In the temperature range of 390–675 °C, the consumption of methane is accompanied by the production of H_2 and CO. Hydrogen is produced via the decomposition of methane over Ni active sites (Eq. (1)) while CO can be formed either by the oxidation of solid carbon (Eq. (3)) and/or by direct partial oxidation of methane (Eq. (4)) in both cases with the participation of lattice oxygen originating from the support.

$$C\,(s) + O\,(s) \rightarrow CO\,(g) \quad (3)$$

$$CH_4\,(g) + O\,(s) \rightarrow CO\,(g) + 2H_2\,(g) \quad (4)$$

The reduction of CH_4 consumption rate observed at the temperature range of 675–850 °C (Fig. 1a) is due to the coverage of active sites by solid carbon (Eq. (1)), however part of methane is still converted probably due to thermal reactions. It should also be noted that in all the temperature range no evolution of C_2H_6 or C_2H_4 was observed, so no dehydration-coupling reactions take place.

The Temperature Programmed methane decomposition reaction profile over Rh(1)CeZrLa is presented in Fig. 2a, while in Fig. 2b a detail of the profile at the initiation of the reaction is shown. Product distribution over Rh(1)CeZrLa is similar to that over Ni(10)CeZrLa with the main difference lying in the reference temperatures (Fig. 1). The initiation of methane consumption is observed at 230 °C accompanied by the production of CO_2 and H_2O with the participation of lattice oxygen. At the temperature of 260 °C H_2 is detected at the outlet of the reactor via the decomposition of methane as well as CO_2 (peak at 400 °C) and CO with the participation of lattice oxygen, probably via the reaction of oxidation of solid carbon (Eq. (3)). At the temperature range of 675–850 °C decrease on the consumption of methane is observed due to the deactivation of the catalyst by the solid carbon accumulation, however part of methane is still consumed via thermal decomposition.

The participation of lattice oxygen of the support during temperature programmed methane decomposition has been reported

Table 1
Microkinetic model for CH_4 steam reforming. Activation energies calculated via the UBI-QEP method using the model parameters' values shown in Table 5. Reported E_a values are for a surface coverage of $\theta_* = 1$.

No.	Reaction	E_a (kJ/mol)		No.	Reaction	E_a (kJ/mol)	
		Ni(10)CeZrLa	Rh(1)CeZrLa			Ni(10)CeZrLa	Rh(1)CeZrLa
R1	$CH_4 + 2^* \rightarrow CH_3^* + H^*$	0.00	0.00	R41	$CHO^* + ^* \rightarrow CH^* + O^*$	134.61	125.92
R2	$CH_3^* + H^* \rightarrow CH_4 + 2^*$	15.38	15.87	R42	$CH^* + O^* \rightarrow CHO^* + ^*$	111.25	123.92
R3	$H_2O + ^* \rightarrow H_2O^*$	0.00	0.00	R43	$CHO^* + ^* \rightarrow CO^* + H^*$	0.00	0.00
R4	$H_2O^* \rightarrow H_2O + ^*$	57.79	59.11	R44	$CO^* + H^* \rightarrow CHO^* + ^*$	99.34	103.12
R5	$H_2O^* + ^* \rightarrow OH^* + H^*$	90.70	91.93	R45	$CHO^* + O^* \rightarrow CO_2^* + H^*$	0.00	0.00
R6	$OH^* + H^* \rightarrow H_2O^* + ^*$	36.58	34.97	R46	$CO_2^* + H^* \rightarrow CHO^* + O^*$	83.65	85.81
R7	$OH^* + ^* \rightarrow H^* + O^*$	71.16	70.07	R47	$CHO^* + O^* \rightarrow CO^* + OH^*$	2.03	1.53
R8	$H^* + O^* \rightarrow OH^* + ^*$	92.14	93.39	R48	$CO^* + OH^* \rightarrow CHO^* + O^*$	80.39	81.33
R9	$OH^* + OH^* \rightarrow H_2O^* + O^*$	0.00	0.00	R49	$CHO^* + CH_2^* \rightarrow CO^* + CH_3^*$	0.00	0.00
R10	$H_2O^* + O^* \rightarrow OH^* + OH^*$	75.10	80.28	R50	$CO^* + CH_3^* \rightarrow CHO^* + CH_2^*$	144.00	128.17
R11	$H_2 + 2^* \rightarrow H^* + H^*$	0.00	0.00	R51	$CHO^* + CH^* \rightarrow CO^* + CH_2^*$	0.00	0.00
R12	$H^* + H^* \rightarrow H_2 + 2^*$	68.96	69.54	R52	$CO^* + CH_2^* \rightarrow CHO^* + CH^*$	110.22	114.19
R13	$CO + ^* \rightarrow CO^*$	0.00	0.00	R53	$CO_2^* + CH^* \rightarrow CO^* + CHO^*$	18.98	28.98
R14	$CO^* \rightarrow CO + ^*$	122.04	123.44	R54	$CO^* + CHO^* \rightarrow CO_2^* + CH^*$	58.04	48.30
R15	$CO_2 + ^* \rightarrow CO_2^*$	0.00	0.00	R55	$CH_2^* + O^* \rightarrow CHO^* + H^*$	15.35	18.50
R16	$CO_2^* \rightarrow CO_2 + ^*$	24.67	24.68	R56	$CHO^* + H^* \rightarrow CH_2^* + O^*$	27.84	9.44
R17	$CH_3^* + ^* \rightarrow CH_2^* + H^*$	88.23	80.86	R57	$CO^* + ^* \rightarrow C^* + O^*$	136.05	137.82
R18	$CH_2^* + H^* \rightarrow CH_3^* + ^*$	43.57	55.81	R58	$C^* + O^* \rightarrow CO^* + ^*$	148.32	146.27
R19	$CH_2^* + ^* \rightarrow CH^* + H^*$	91.94	93.07	R59	$CO^* + H^* \rightarrow C^* + OH^*$	99.60	102.09
R20	$CH^* + H^* \rightarrow CH_2^* + ^*$	81.06	82.00	R60	$C^* + OH^* \rightarrow CO^* + H^*$	90.89	87.22
R21	$CH^* + ^* \rightarrow C^* + H^*$	28.12	38.82	R61	$CO^* + CO^* \rightarrow C^* + CO_2^*$	13.65	16.38
R22	$C^* + H^* \rightarrow CH^* + ^*$	163.10	152.40	R62	$C^* + CO_2^* \rightarrow CO^* + CO^*$	10.24	7.52
R23	$CH_3^* + O^* \rightarrow CH_2^* + OH^*$	108.29	100.88	R63	$CO_2^* + H^* \rightarrow CO^* + OH^*$	43.86	44.44
R24	$CH_2^* + OH^* \rightarrow CH_3^* + O^*$	42.65	52.51	R64	$CO^* + OH^* \rightarrow CO_2^* + H^*$	38.57	38.43
R25	$CH_2^* + O^* \rightarrow CH^* + OH^*$	102.13	103.93	R65	$CO^* + H^* \rightarrow CH^* + O^*$	184.28	177.48
R26	$CH^* + OH^* \rightarrow CH_2^* + O^*$	70.27	69.53	R66	$CH^* + O^* \rightarrow CO^* + H^*$	61.58	72.36
R27	$CH^* + O^* \rightarrow C^* + OH^*$	38.25	49.53	R67	$CO_2^* + ^* \rightarrow CO^* + O^*$	40.24	39.86
R28	$C^* + OH^* \rightarrow CH^* + O^*$	152.25	139.78	R68	$CO^* + O^* \rightarrow CO_2^* + ^*$	55.93	57.17
R29	$CH_3^* + OH^* \rightarrow CH_2^* + H_2O^*$	95.56	91.93	R69	$COOH^* + ^* \rightarrow CO^* + OH^*$	34.32	36.48
R30	$CH_2^* + H_2O^* \rightarrow CH_3^* + OH^*$	105.02	123.84	R70	$CO^* + OH^* \rightarrow COOH^* + ^*$	48.11	46.39
R31	$CH_2^* + OH^* \rightarrow CH^* + H_2O^*$	53.85	53.75	R71	$COOH^* + ^* \rightarrow CO_2^* + H^*$	1.70	3.29
R32	$CH^* + H_2O^* \rightarrow CH_2^* + OH^*$	97.09	99.64	R72	$CO_2^* + H^* \rightarrow COOH^* + ^*$	20.79	19.21
R33	$CH^* + OH^* \rightarrow C^* + H_2O^*$	0.00	1.46	R73	$CO^* + H_2O^* \rightarrow COOH^* + H^*$	97.10	66.87
R34	$C^* + H_2O^* \rightarrow CH^* + OH^*$	189.10	172.00	R74	$COOH^* + H^* \rightarrow CO^* + H_2O^*$	29.19	0.00
R35	$CH^* + CH^* \rightarrow CH_2^* + C^*$	52.13	66.92	R75	$CO_2^* + OH^* \rightarrow COOH^* + O^*$	79.63	77.61
R36	$CH_2^* + C^* \rightarrow CH^* + CH^*$	197.99	191.56	R76	$COOH^* + O^* \rightarrow CO_2^* + OH^*$	81.53	85.01
R37	$CH_2^* + CH^* \rightarrow C^* + CH_3^*$	0.00	12.15	R77	$CO_2^* + H_2O^* \rightarrow COOH^* + OH^*$	99.59	99.64
R38	$C^* + CH_3^* \rightarrow CH_2^* + CH^*$	179.64	150.78	R78	$COOH^* + OH^* \rightarrow CO_2^* + H_2O^*$	26.38	26.76
R39	$CH_2^* + CH_2^* \rightarrow CH_3^* + CH^*$	57.87	68.54				
R40	$CH_3^* + CH^* \rightarrow CH_2^* + CH_2^*$	91.65	82.52				

Table 2
Characteristic properties of the catalysts and the supports.

Sample	Metal loading (wt%)	Specific surface area (m^2/g)	Dispersion (%)	Metal surface area (m^2_M/g_{cat})	$T_{maxred.}$ (°C)
Ni(10)CeZrLa	Ni-10%	37	1.2	0.80	480
Rh(1)CeZrLa	Rh-1%	42	19.0	0.85	180
CeZrLa support	–	62	–	–	340

in literature [51,52], where the production of either CO_2 or CO was attributed to (partial) oxidation of methane over ceria. The production of CO instead of CO_2 has been related to the availability and diffusion rate of lattice oxygen [52]. At the beginning of the reaction, surface lattice oxygen is participating to the production of CO_2, while the production of CO has been related to the participation of lattice oxygen controlled by the diffusion of bulk lattice oxygen. It has also been found over $Rh/Ce_\alpha Zr_{1-\alpha}O_2$ catalyst that the support provides actives sites for the activation of steam and that the surface reactions between carbon containing species and the lattice oxygen leading to the formation of CO and CO_2 are rate limiting [53].

In order to elucidate whether the formation of CO_2 and CO in temperature programmed methane decomposition experiments takes place directly over active sites of the support or indirectly on the active sites of the metal, the same test was realized over the bare CeZrLa support. The conversion of methane during temperature programmed methane decomposition experiments over the two catalysts and the bare support are shown in Fig. 3.

It is clear that methane cannot be activated over the bare support since the only conversion observed is that of thermal decomposition of methane at temperature higher than 750 °C. Therefore, the activation of methane on the metal is required and direct (partial) oxidation of methane on the support can be excluded. The participation of lattice oxygen in the formation of CO_2 and CO is probably induced by strong interactions of the metal with the ceria-containing support. It has been previously reported that strong metal-support interactions, cause Rh to lose its metallic character [54] and lead to the formation of $Rh^0/Rh^{+\delta}$ and Ce^{+4}/Ce^{+3} redox couples [55]. Analogous findings are reported by Carrasco et al. [56] based on DFT calculations on $Ni/CeO_2(111)$ where SMSI cause partial oxidation of Ni by ceria which is partially reduced. As a result, active lattice oxygen is believed to be transferred from the support to the metal, where it reacts with carbon species and leads to the formation of CO_2 and CO. The notable difference in the reaction

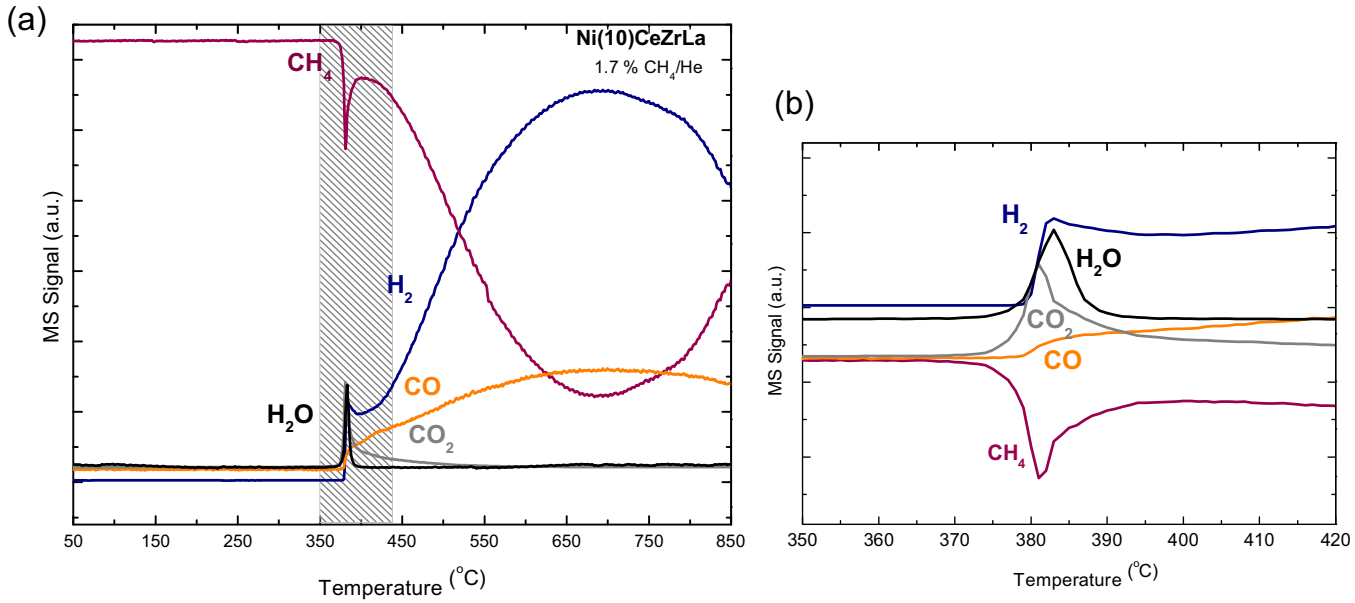

Fig. 1. (a) Profile of Temperature Programmed Methane Decomposition Reaction over Ni(10)CeZrLa (b) Detail close to ignition temperature (highlighted area). Reaction gas composition: 1.7% CH_4/He.

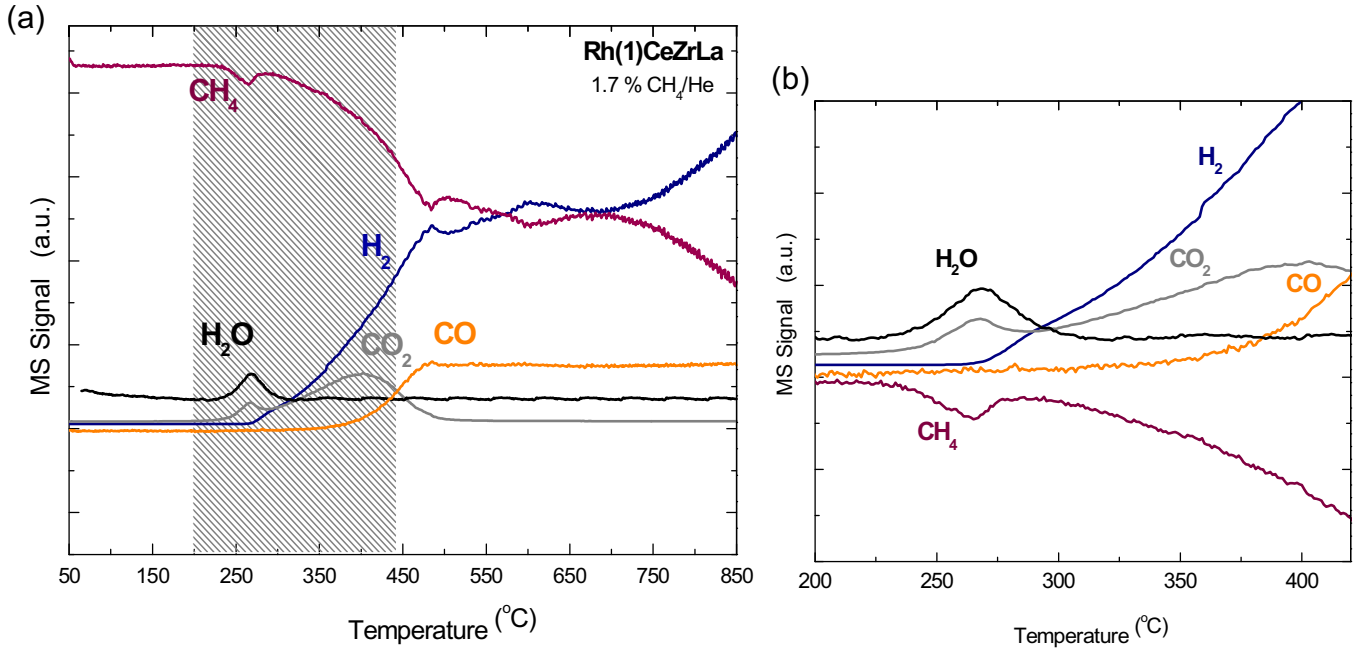

Fig. 2. (a) Profile of Temperature Programmed Methane Decomposition Reaction over Rh(1)CeZrLa (b) Detail close to ignition temperature (highlighted area). Reaction gas composition: 1.7% CH_4/He.

initiation temperatures over Ni and Rh based catalysts further supports the above conclusion, demonstrating the decisive role of the metal in methane activation.

3.3. KIE results – H_2O effect

Information on the mechanism and the steps that are kinetically relevant can be provided via the investigation on the kinetic isotope effect. The kinetic isotope effect is referred to the effect on the reaction rate due to isotopic replacement of one or more bonds of the reactant. More specifically, when isotopic exchange refers to the replacement of hydrogen with deuterium, the properties of the bond are significantly affected. For the cleavage of a C—D bond, higher energy is required with respect to that for the C—H bond [57]. As a result, if the consumption rate of the C—H containing reactant is experimentally found to be higher than that of the C—D-containing reactant (normal kinetic isotope effect KIE = $k_H/k_D > 1$), then the cleavage of a C—H bond is involved in the rate controlling step [58].

The investigation of the kinetic isotope effect was realized through temperature programmed steam reforming and methane decomposition experiments using either CH_4 or CD_4 in the reaction mixture. The intrinsic consumption rates of CH_4 and CD_4 during temperature programmed steam reforming experiments over Ni(10)CeZrLa and Rh(1)CeZrLa with steam to methane ratio of 2 or 3 are presented in Fig. 4. It is obvious that for both catalysts the con-

Table 3
Kinetic Isotope Effect over Ni(10)CeZrLa and Rh(1)CeZrLa.

Catalyst	Temperature (°C)	Steam reforming (S/C = 2)	Steam reforming (S/C = 3)	CH_4 decomposition
Ni(10)CeZrLa	500	1.5	1.4	1.3
Rh(1)CeZrLa	450	–	1.5	1.6

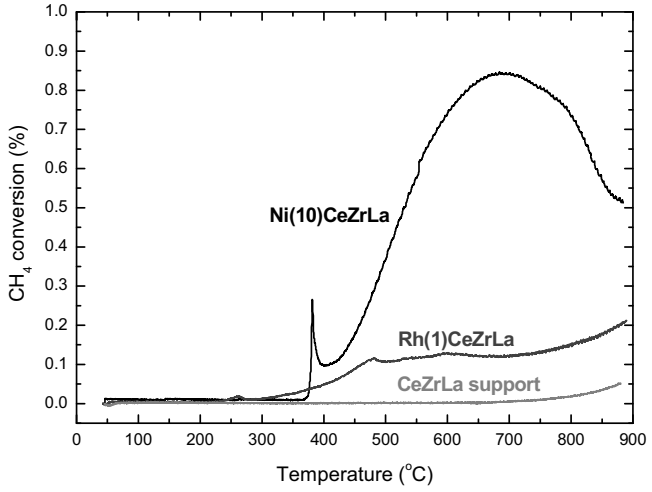

Fig. 3. Methane conversion during temperature programmed methane decomposition over the catalysts and the support. Reaction gas composition: 1.7% CH_4/He.

sumption rate of CH_4 is higher than that of CD_4 in the temperature range of interest (400–550 °C). Therefore it is clear that the steps that limit the overall reaction rate include the cleavage of a C—H bond. The calculated kinetic isotope effect at 500 °C and S/C = 3 is normal and equal to 1.4 and 1.5 for Ni and Rh respectively (Table 3).

However, the fact that a C—H bond is activated within a kinetically important step does not necessarily mean that steam-derived intermediates are not also involved. In order to get more information on this aspect, temperature programmed steam reforming experiments at different S/C ratio were carried over Ni(10)CeZrLa (Fig. 4a). It is observed that the intrinsic consumption rate of methane (either CH_4 or CD_4) is not affected by the S/C ratio, thus a steam independent kinetically important step is evident. Furthermore, the role of steam derived intermediates in the kinetically important steps was investigated following the methodology of Wei and Iglesia [20]. In that work, the activation energies, the kinetic parameters and the kinetic isotope effects of steam and dry reforming at 600 °C were found to be similar to methane decomposition reaction concluding that the rate determining step includes the activation of a C—H bond and that the co-reactant (steam or CO_2) does not participate in the kinetically relevant steps. Accordingly, the results of the investigation of the kinetic isotope effect of the methane decomposition reaction over Ni(10)CeZrLa and Rh(1)CeZrLa are shown in Fig. 5a and b.

In the temperature programmed test of methane decomposition reaction using CD_4 instead of CH_4 (Fig. 5b), the ignition temperature is observed at 470 °C in a sharp peak of methane consumption which is attributed to oxidation reactions with the participation of lattice oxygen as described in Section 3.2. The higher temperature this peak is observed is indicative of the higher energetic needs for the cleavage of the C—D versus the C—H bond. After the sharp peak of methane consumption, the intrinsic rate of CD_4 is lower than that of CH_4, indicating a normal kinetic isotope in methane decomposition reaction over Ni(10)CeZrLa. At the temperature of 500 °C the kinetic isotope effect was 1.3, a value almost equal to the kinetic isotope effect determined for the steam reforming reaction (within experimental error). Similar results were obtained over

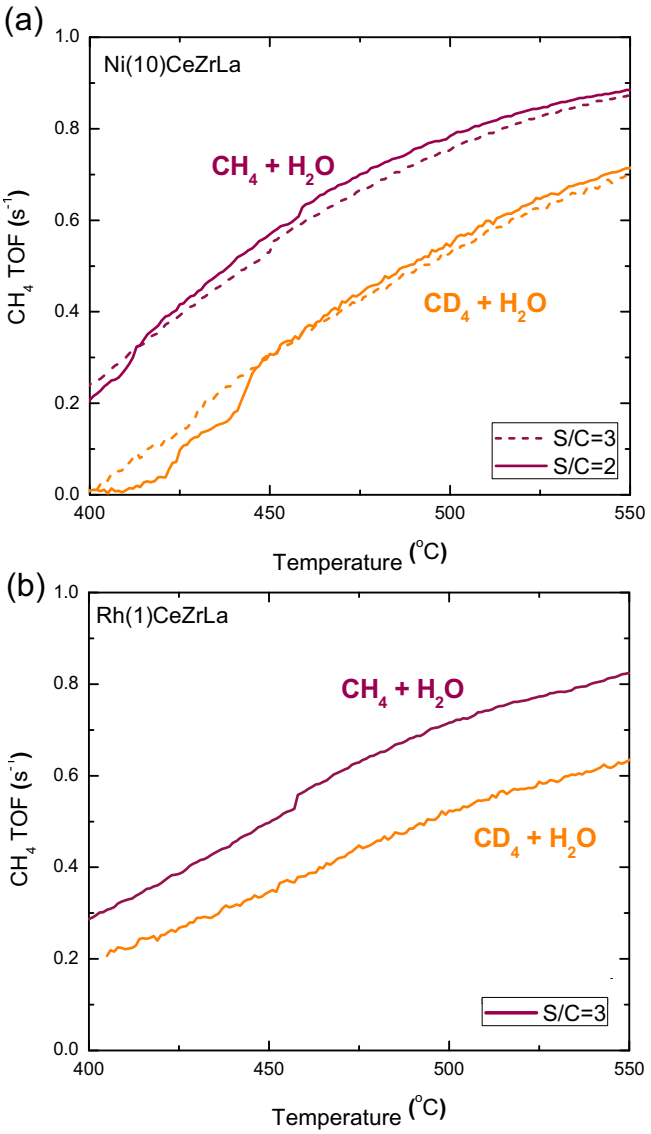

Fig. 4. Intrinsic consumption rate of CH_4 and CD_4 during temperature programmed steam reforming over (a) Ni(10)CeZrLa and (b) Rh(1)CeZrLa. Conditions: 1.7% CH_4 (CD_4) and 3.4% H_2O (S/C = 2) or 5.1% H_2O (S/C = 3) on He.

Rh(1)CeZrLa catalyst as shown in Fig. 5b. For the determination of the kinetic isotope effect of methane decomposition, the temperature range of 400–450 °C is used, which corresponds to the period after the sharp peak of methane consumption due to oxidation reactions with the participation of lattice oxygen. The temperature of 450 °C was used as reference temperature for the calculation of the kinetic isotope effect in order to avoid possible influence of deactivation of the catalyst due to solid carbon accumulation. It is stressed that one of the products of methane decomposition reaction is solid carbon, which may deactivate the catalyst at short time, especially when the metal loading is as low as in Rh(1)CeZrLa. At the temperature of 450 °C, the kinetic isotope effect was 1.6 (Table 3), almost as that of steam reforming reaction at the same temperature (within

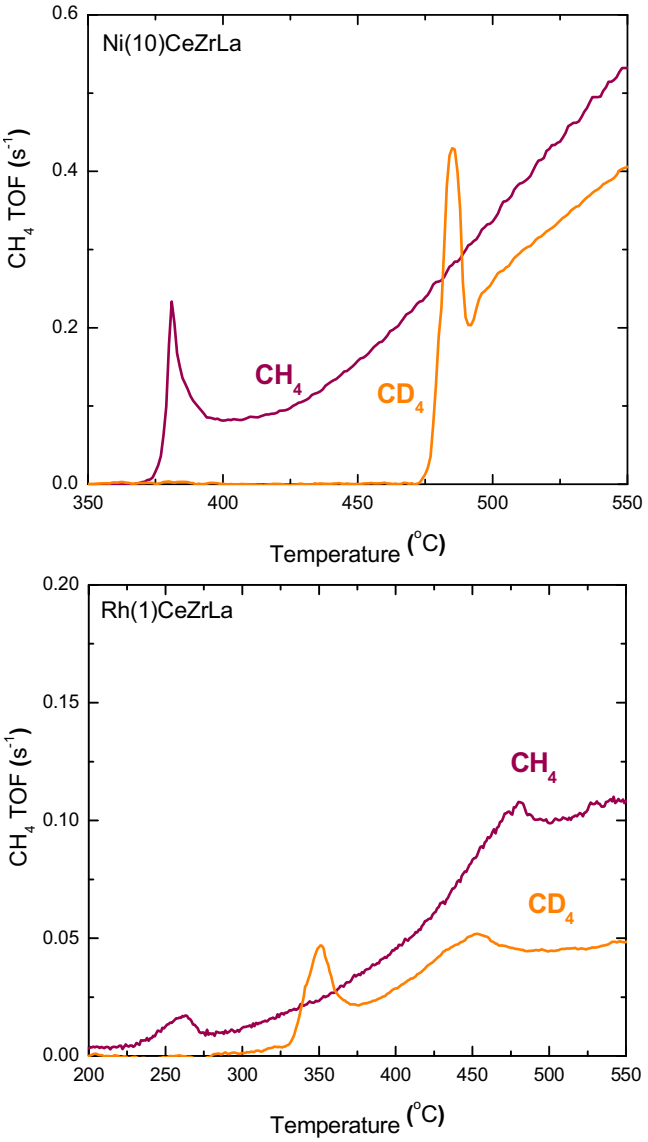

Fig. 5. Intrinsic consumption rate of CH_4 and CD_4 during temperature programmed methane decomposition over (a) Ni(10)CeZrLa and (b) Rh(1)CeZrLa. Conditions: 1.7% CH_4 (CD_4) on He.

experimental error). It is, therefore, evident that the steps that are kinetically important over both Ni(10)CeZrLa and Rh(1)CeZrLa are the same for the two reactions and no steam-derived intermediates are expected to be involved. The possibility that oxygen diffusion from the bulk of the support to the surface affects the overall rate during decomposition cannot be excluded, however it is the metal presence that clearly drives the dehydrogenation of methane forming CH_x, further oxidized to CO_x by lattice oxygen. During steam reforming mode, surface oxygen is either available on the metal itself or is very quickly replenished by steam activation on the support and, as such, the potential rate control of oxygen transfer is negligible. Summarizing, the values of the kinetic isotope effect calculated for the steam reforming and the methane decomposition reaction over the two catalysts are presented in Table 3.

There are very few studies of the kinetic isotope effect of steam reforming reaction at the low temperature range. The kinetic isotope effect calculated in this work are in agreement with the available literature. At 600 °C the kinetic isotope effect over a $Ni/NiAl_2O_4$ catalyst at S/C of 3.6 was 1.3 [41,59], over a Ni/MgO was 1.66 [20] and over a Rh/Al_2O_3 catalyst was 1.54 [21]. For the reaction of dry reforming the kinetic isotope effect was found to be 1.45 over a Ni/Al_2O_3 catalyst at 600 °C [60], while for the reaction of methane decomposition at 500 °C in the presence of Ni/SiO_2 the kinetic isotope effect was 1.45 [61]. The use of a reducible support in the current work could be responsible for electronic modifications of the metal, however the very similar KIE values measured over both metals and reaction modes and the good agreement with literature values, strongly suggests the dominating role of the metal. Further support is provided via modelling results presented below.

3.4. Model validation

The above isotopic evidence from temperature programmed experiments are further probed through the microkinetic modelling results discussed in the following sections, aiming at the elucidation of the kinetic relevance of surface steps and their participation in the major reaction pathways. The current microkinetic model is fully defined on the basis of 17 parameters, 12 heats of chemisorption and 5 sticking coefficients, with all kinetic parameters being correlated to these variables. For the simulation of the experiments presented in Angeli et al. [19] a separate set of model parameters for Ni(10)CeZrLa and Rh(1)CeZrLa was estimated via regression. Initial guesses for heats of chemisorption were selected based on reported values for Ni(111) and Rh(111) [48], while a value of 1 was chosen to initialise the sticking coefficients for both catalysts. The estimated values for the model parameters for both catalysts are presented in Table 5 and will be discussed in detail in Section 3.8, while in this section the discussion focuses mainly on the description of the experimental results by the model.

In Fig. 6 parity diagrams are provided for all gas-phase species, where the overall satisfactory agreement in the entire range of experimental conditions between the model predicted and experimental results can be seen for both catalysts. The description of the outlet molar fraction of CH_4 and H_2O is particularly good, indicating that the main activation and conversion pathways of the primary reactants are described properly by the developed model. CO appears to be the component with, comparatively, the most noticeable deviations, a fact that can be associated with the lower order of magnitude of its molar fraction and the associated experimental measurement uncertainty at this range. CO_2 and H_2, being the main, quantitatively, steam reforming products at the low investigated experimental temperatures, display similar qualitative trends. Besides a slightly wider scatter for CO_2 and H_2 over the Rh catalyst, no particular qualitative differences can be identified in the simulation of the two catalysts, indicating that the model was able to capture properly the trends of the experimental data for both materials.

Fig. 7 shows the effect of temperature, H_2O/C ratio and GHSV at selected conditions on the conversion of CH_4 and H_2O, as well as on the selectivity towards CO and CO_2 for the two catalysts evaluated. As seen in this figure, all experimental trends are reproduced well by the microkinetic model using the parameters reported in Table 5 for both catalysts. As expected, an increase in temperature (panels (a) and (b)) leads to a rise in both reactants conversion and a drop in CO_2 selectivity. The latter is logically accompanied by a respective increase in the selectivity of CO, an effect that is observed to be more pronounced over the Ni catalyst. This behaviour is accurately described by the model, indicating that the two catalysts are successfully discriminated in the current results and that the surface pathways leading to products formation have been properly described. The inlet H_2O/C ratio positively affects the CH_4 conversion and the CO_2 selectivity, while the inverse holds for H_2O conversion and the CO selectivity, as seen in panels (c) and (d) of Fig. 7. Again, the experimental trends are reproduced correctly in the modelling results, suggesting that the activation processes of both reactants have been accurately captured. Moreover, consider-

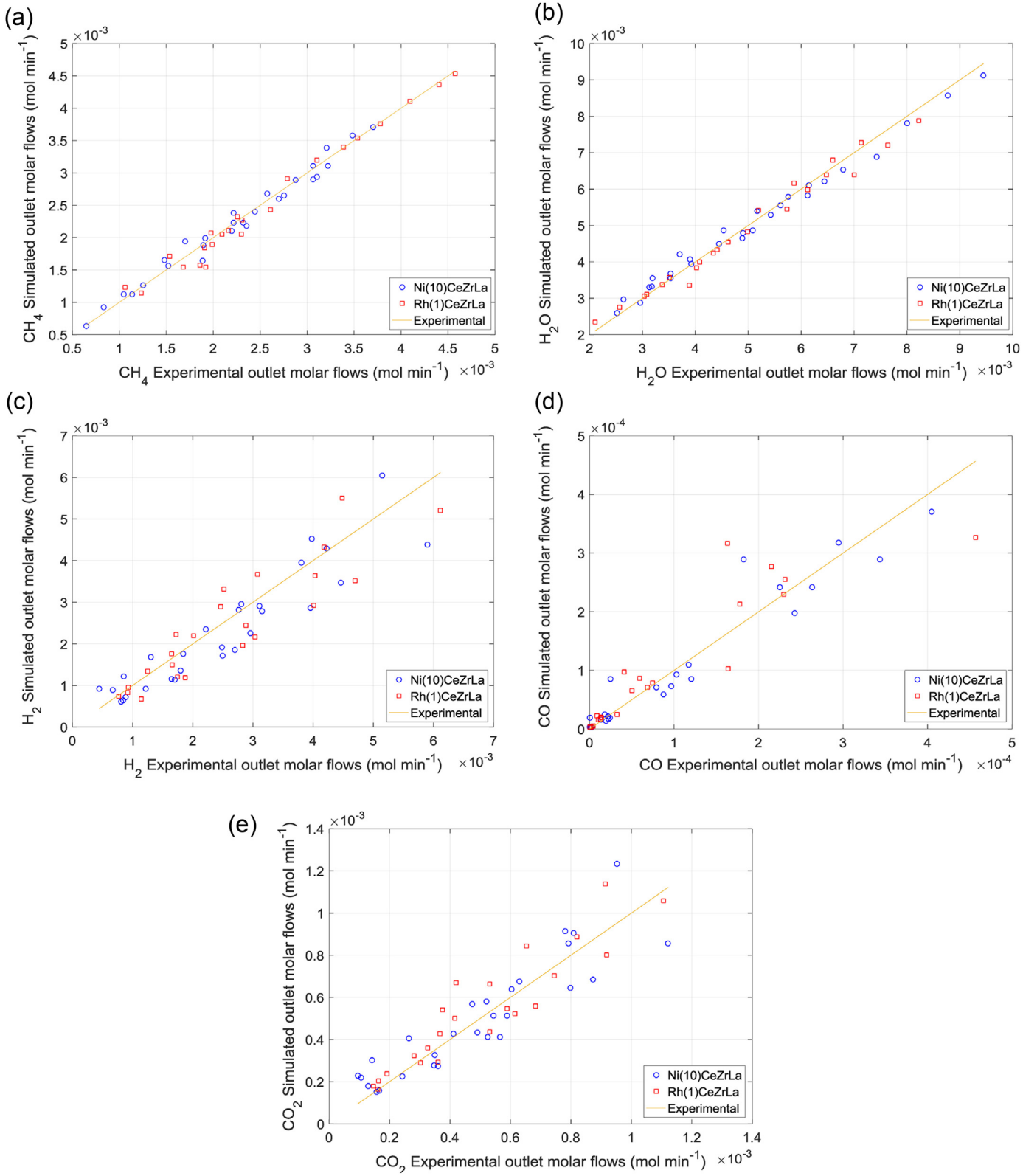

Fig. 6. Parity diagrams for all gaseous components over the Ni(10)CeZrLa and Rh(1)CeZrLa catalysts. Experimental conditions are summarised in Section 2.1.2 and discussed in Ref. [19], while modelling results have been obtained with the parameters' values shown in Table 5.

ing the experimentally observed kinetic irrelevance of steam during isotopic studies (see Section 3.3), the current simulation results further suggest that thermodynamic effects are appropriately considered in the model. Finally, in panels (e) and (f) the effect of space velocity is depicted. Qualitatively, trends simulation is adequate, however the model appears to underestimate the strength of this parameter's effect on the conversion of CH_4, especially on Rh. This could be an indication that, for example, some of the assumptions made during the development of the model in relation to the mobility of the surface species require some refinement or further tuning.

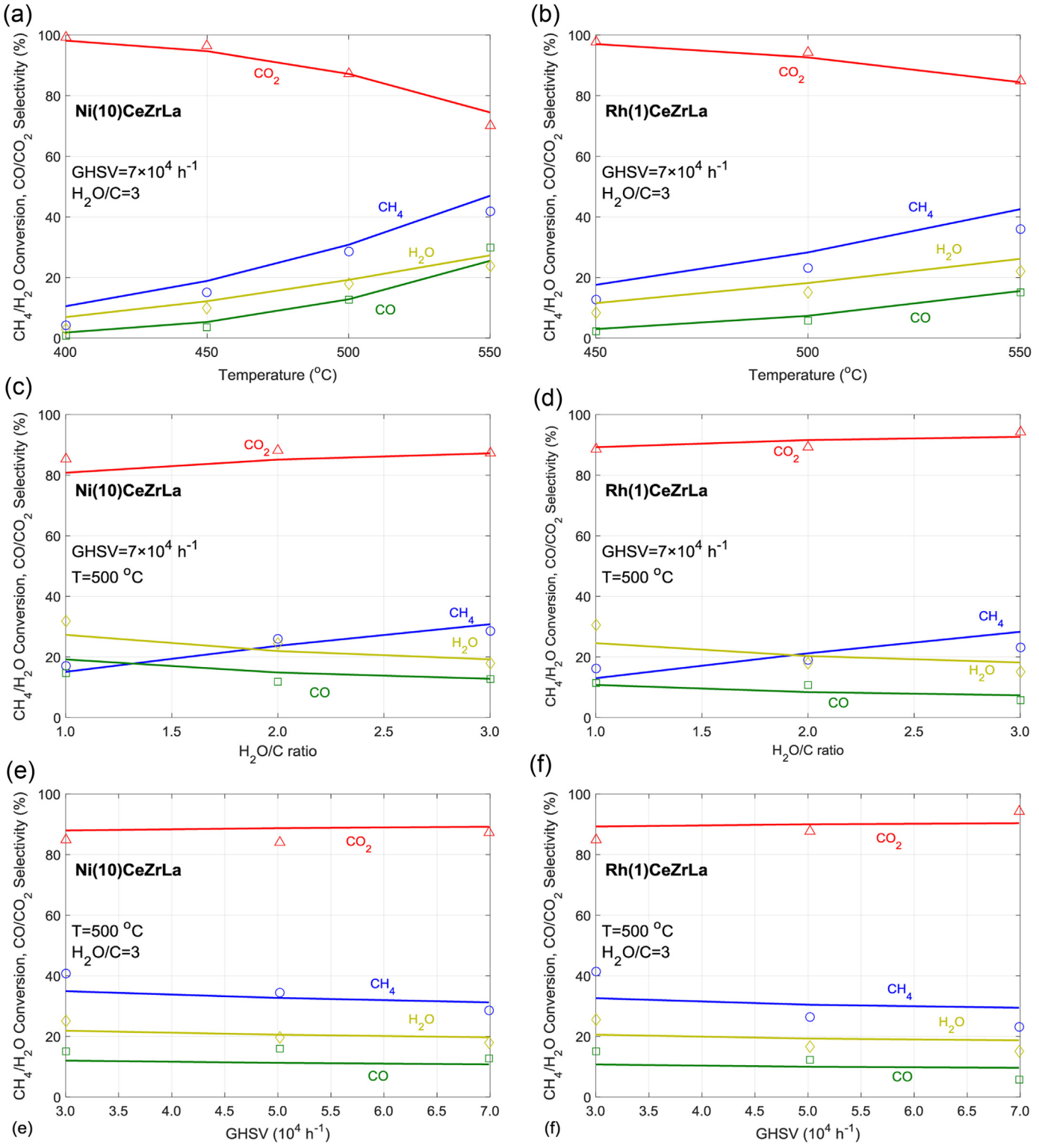

Fig. 7. Comparison of model predicted conversions and selectivities over Ni(10)CeZrLa and Rh(1)CeZrLa (lines) with experimental results (symbols). Operating conditions are indicated on the respective panels, while modelling results have been obtained with the parameters' values shown in Table 5.

Nonetheless, the overall good agreement of the model results with the experimental ones for both catalysts, as shown in the discussion of this section, provides confidence on further using the model to evaluate the kinetic importance of reaction steps and investigating whether model predictions are in agreement with the temperature programmed isotopic results presented above.

3.5. Kinetic relevance of reaction steps

In order to elucidate the kinetic relevance of surface elementary steps, a sensitivity analysis (SA) was conducted with respective results being presented below. The pre-exponential factors of each reaction pair (forward-backward) were perturbed by a small fraction of their base value and the effect on reactants conversion

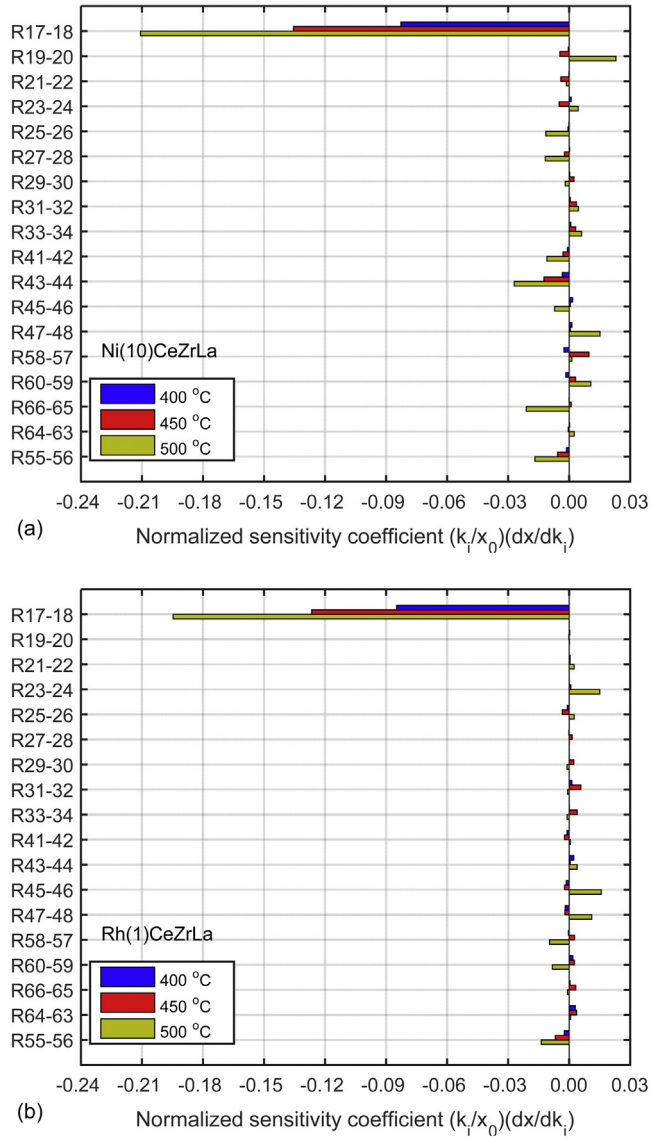

Fig. 8. Sensitivity analysis of pre-exponential factors of most relevant reactions considered in the microkinetic model shown in Table 1 for (a) Ni(10)CeZrLa and (b) Rh(1)CeZrLa at different reaction temperatures. Base values for pre-exponential factors are calculated as described in the Supporting Information. Operating conditions: GHSV = 7×10^4 h^{-1}, $H_2O/C = 3$.

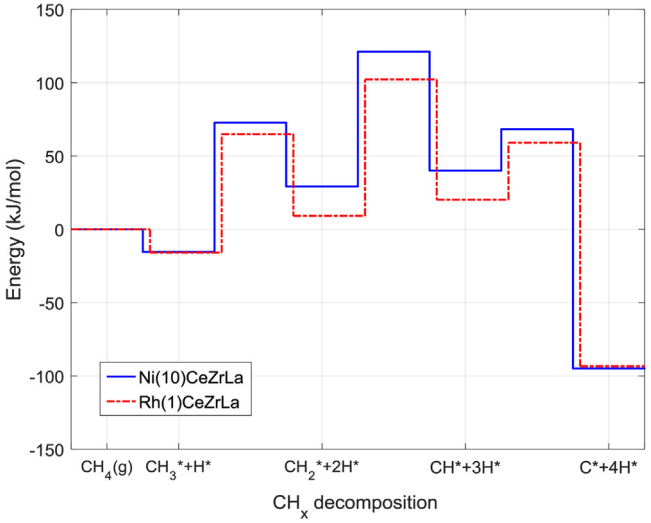

Fig. 9. Energetics of the CH_x dehydrogenation pathway for Ni(10)CeZrLa and Rh(1)CeZrLa as calculated via the UBI-QEP method using the model parameters' values shown in Table 5.

and products selectivity was quantified by means of calculating first-order normalised sensitivity coefficients. Fig. 8 presents the sensitivity analysis results for CH_4 conversion for both materials studied at three different temperatures. Only the most relevant reactions in terms of kinetic relevance, as identified in existing literature, are shown. Namely, methane adsorption and the subsequent dehydrogenation and oxidative dehydrogenation steps, have typically been considered as rate determining [35,62], along with steps leading to the formation of C—O and OC—O bonds [62]. The latter have been found to take place via oxidation reactions of either the bare carbon atom C* [26,36] or a CH_x* [35,36] intermediate. Moreover, temperature has been discussed to potentially have a major impact of the nature of the rate determining step [26,36], and, specifically, the importance of pathways based on the formyl intermediate at low temperatures has been highlighted [36]. As seen in Fig. 8, most important reaction step identified via the sensitivity analysis is the dehydrogenation of CH_3* (R17). This holds for both the Ni and the Rh catalyst across the temperature range evaluated, with the sensitivity of the reaction increasing with rising temperature. All other steps are clearly not kinetically relevant at these conditions based on this analysis. The same holds also for the rest of the steps considered in the kinetic model given in Table 1 that are not displayed in this figure. As discussed in Section 3.3, the CH_4/CD_4 temperature programmed steam reforming experiments demonstrated a normal kinetic isotope effect for the Ni and Rh catalysts, suggesting that a C—H bond cleavage would be expected to participate in the rate-determining step in both cases. Moreover, given the observed lack of an effect of the partial pressure of steam on the conversion of CH_4 or CD_4 in the same experiments over the Ni catalyst and the overall consistent KIE value calculated over Ni and Rh during steam reforming and decomposition reaction modes, it was concluded that steam-derived intermediates are not participating in the kinetically relevant step(s). The SA results agree very well with these experimental observations, since step R17 fulfils all these requirements and is clearly the most sensitive reaction. Similar simulation results have been reported for the case of Rh catalysts by Maestri et al. [29] and, as already commented, are in line with reported experimental evidence over both Ni [20] and Rh [21] catalysts.

Furthermore, given the above experimental evidence on the nature of the rate determining step, the activation energies calculated through UBI-QEP along the CH_x* dehydrogenation pathway have also been considered (Fig. 9), since the respective steps would all satisfy the stipulated characteristics. Steps $CH_3^* + * \rightarrow CH_2^* + H^*$ (R17) and $CH_2^* + * \rightarrow CH^* + H^*$ (R19) are revealed to have equally high activation energies for the Ni catalyst, while for the Rh catalyst it is step $CH_2^* + * \rightarrow CH^* + H^*$ that appears to have the highest activation energy. If the CH_x* dehydrogenation pathway belongs to the main reaction pathway, meaning that CO and CO_2 formation stem from C* oxidation, these results would imply a kinetic relevance of CH_2* dehydrogenation. However, the latter fact is not evidenced from the SA results presented above. Additionally, the model predicts step R19 to be closer to equilibrium compared to R17, as indicated through an evaluation of the partial equilibrium ratio of these reaction pairs (Table 4). The latter parameter is defined as the ratio of the forward to the sum of forward and backward rate, $r_i^f / \left(r_i^f + r_i^b\right)$, and describes whether the reaction is in partial equilibrium or if it proceeds in the forward or reverse direction [29]. As seen in this table, the adsorption of CH_4 and the dehydrogenation of CH* are consistently at equilibrium, while CH_3* and CH_2* dehydrogenations are always shifted in the forward direction, with the

Table 4
Partial equilibrium approach of CH_x* dehydrogenation reaction steps. Operating conditions: GHSV = 7×10^4 h^{-1}, $H_2O/C = 3$.

Temperature (°C)	Ni(10)CeZrLa				Rh(1)CeZrLa			
	R1–2	R17–18	R19–20	R21–22	R1–2	R17–18	R19–20	R21–22
550	0.50	0.86	0.77	0.50	0.50	0.72	0.62	0.51
500	0.50	0.90	0.83	0.50	0.50	0.78	0.66	0.51
450	0.50	0.93	0.88	0.51	0.50	0.85	0.72	0.51
400	0.50	0.95	0.94	0.51	0.50	0.70	0.60	0.51

Table 5
Estimated model parameters and 95% confidence intervals for Ni(10)CeZrLa and Rh(1)CeZrLa catalysts.

Parameter		Ni(10)CeZrLa	Rh(1)CeZrLa
Q_{H_2O}	(kJ/mol)	57.87 ± 0.37	59.15 ± 0.55
Q_{CO}	(kJ/mol)	122.04	123.44
Q_{CO_2}	(kJ/mol)	24.67	24.68
Q_{CH_3}	(kJ/mol)	207.10 ± 1.53	207.40 ± 3.72
Q_{CH_2}	(kJ/mol)	372.24 ± 1.93	391.73 ± 3.72
Q_{CH}	(kJ/mol)	537.03	556.07
Q_C	(kJ/mol)	763.05 ± 0.95	761.30 ± 1.88
Q_{CHO}	(kJ/mol)	208.78	206.69
Q_{OH}	(kJ/mol)	253.91	252.10
Q_O	(kJ/mol)	453.45	453.68
Q_H	(kJ/mol)	255.82 ± 1.63	255.51 ± 4.25
Q_{COOH}	(kJ/mol)	250.01	253.47
S_{CH_4}	(−)	1.00	1.00
S_{H_2O}	(−)	1.00	1.00
S_{CO}	(−)	$1.57 \pm 0.01 \times 10^{-3}$	$2.62 \pm 0.03 \times 10^{-3}$
S_{CO_2}	(−)	1.00	1.00
S_{H_2}	(−)	$1.83 \pm 0.03 \times 10^{-3}$	$3.02 \pm 0.04 \times 10^{-3}$

effect being more pronounced for the former species. The relative approach to equilibrium of these two steps, in combination with the SA and experimental results, again draws step R17 as the most kinetically relevant step both for Ni and Rh. The latter aspect will be further clarified in the following section, where the steps comprising the main reaction pathways are discussed. Finally, it bears attention that, as will also be elaborated below, Fig. 9 provides a first indication of the more favourable energetics of the steam reforming reaction over Rh in comparison to Ni, a fact that is in further agreement with available literature.

3.6. Reaction pathway analysis

A differential contribution analysis at the outlet of the catalyst bed is conducted to elucidate the importance of the various reaction pathways. Results for the considered catalyst materials are summarized in Fig. 10, accounting for the net formation rates of all involved gas-phase molecules and surface species. The complexity of the reaction pathways for both metals is clear, however a common preferred pathway can be identified. The discussion below reports quantitative results primarily based on the Ni catalyst, however the dominant pathways qualitatively are the same on Rh with only variable differences at relative contributions of the involved reactions.

According to the predictions of the model, CH_4 adsorbs dissociatively on the catalyst via reaction R1, giving rise to CH_3* surface species. The analysis reveals all gas phase molecules, including methane as seen also in Table 4, to be in equilibrium with their adsorbed state. CH_3* species further dehydrogenate towards CH_2*, as discussed in Section 3.5, via reaction R17 that is found to be the primary pathway for this conversion with a contribution higher than 99.9% at these conditions. Formed CH_2* species, reacting with O* according to step R55, are almost exclusively converted to CHO*, which the current model reveals to be a key surface intermediate in the overall reaction pathway. In the study of Blaylock et al. [36] CHO* was also identified as important for the formation of CO*, especially over the Ni(211) facet, although in that work it was primarily produced via the oxidation of CH* rather than CH_2*. In the current work, more than 99.9% of the CH_2* species reacts via step R55 to form CHO* over Ni(10)CeZrLa, while over Rh(1)CeZrLa this step is also dominant accounting for 85.3% of CH_2* conversion. On the Rh catalyst, a small percentage of CH_2* (8.5%) is also predicted to dehydrogenate towards CH*, which, as will further be discussed in Section 3.8, can be associated with the relatively stronger binding of CH* estimated for this catalyst in comparison to Ni (see Table 5). Following its formation, CHO* dissociates primarily via reaction R43 (≈96%), leading to the formation of CO* and H* species, while minor contributions are calculated also from dissociation reaction R41 towards CH* and O*. CO* is predicted to follow multiple pathways. Its reaction with H_2O* and OH*, according to steps R73 and R70 at contributions of roughly 8 and 5% respectively, leads to the formation of COOH*, while through step R64, CO* further reacts at a small degree (≈3%) with OH* producing CO_2*. Nonetheless, CO* disproportionation (reaction R61) is found to have a substantial role towards the productions of CO_2* and C*, being responsible for the conversion of approximately 80% of CO*. Finally, to a lesser extent CO* obviously desorbs giving rise to gas phase CO. Through its dissociation via reaction R71, COOH* is a primary species in the CO_2* production pathway, the latter desorbing almost exclusively in the gas phase for CO_2 production. Apart from the already commented reactions R64, R61 and R71, minor contributions to the production of CO_2* are also predicted by the model through CHO* oxidation according to reaction R45.

The remaining carbon containing species considered in the model are revealed to be of secondary importance to the main production pathways, nonetheless they participate in a variety of reactions at varying levels contributing to the production or consumption of the main surface intermediates. CH* is mainly formed through the dehydrogenation of CH_2* (directly or with OH* according to steps R19 and R31) and almost exclusively decomposes towards C* via reaction R21. R19, hence, is not part of the dominant reaction pathway, explaining the lack of sensitivity to the reaction identified above. The main pathway for C* generation is not through R21, though, but via the disproportionation of CO*. C* on the catalyst surface gets actually consumed solely towards CO* through its oxidation by OH* according to reaction R60.

As far as non-carbon containing surface intermediates are concerned, model predictions show that steam following its molecular adsorption, gives rise to H_2O* species that predominantly decompose towards OH* and H* following reaction R5 (≈67%), with the aforementioned reaction R73 accounting for the remaining of its consumption rate. Interestingly, apart from the various OH* involving reactions discussed above, it is the recombination of hydroxyl surface species (reaction R9) that accounts for its consumption to a large extent (≈55%), with O* actually being formed mainly through this reaction. The key reaction step R55 discussed above leading to CHO* formation from CH_2* is the major O* consuming step. Finally, formed H* species associatively desorb for the production of gaseous hydrogen.

In summary, the reaction pathway analysis results presented above further provide support and are in agreement with the kinetic isotope effects observed during the temperature pro-

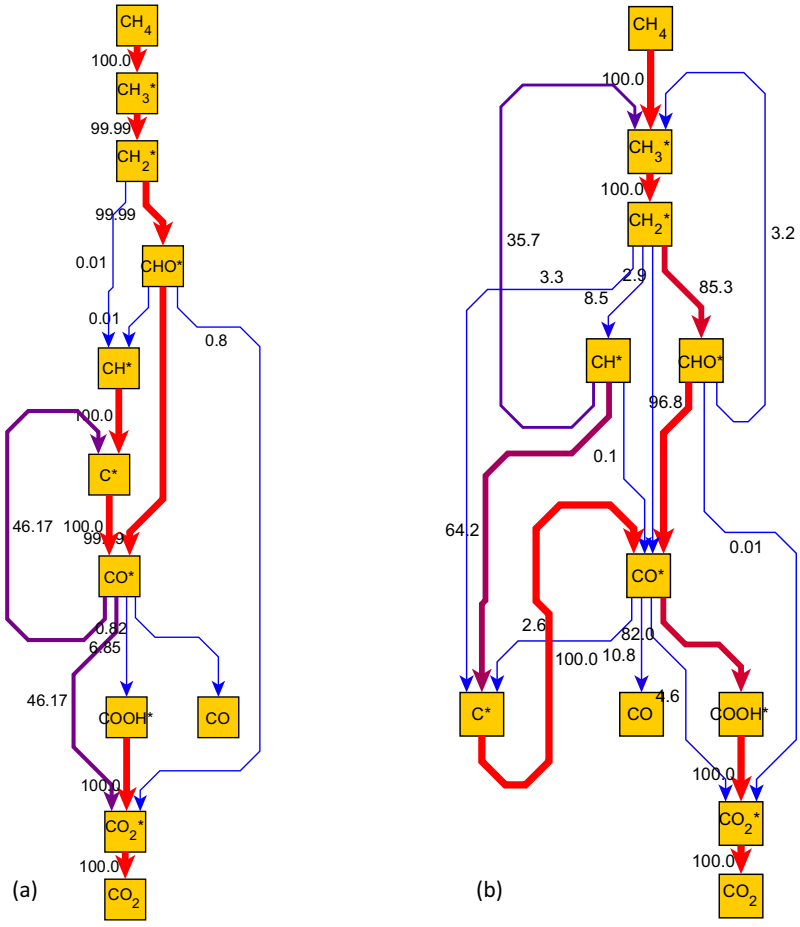

Fig. 10. Contribution analysis for (a) Ni(10)CeZrLa and (b) Rh(1)CeZrLa at the end of the catalyst bed. Net production rates of carbon containing species are considered to calculate conversion percentages towards other compounds. Colour mapping and line thickness are used to indicate a higher conversion percentage, with blue representing the lowest considered value (0.0%) and red the highest value for conversion (100%). Operating conditions: GHSV = 7×10^4 h^{-1}, T = 450 °C, $H_2O/C = 3$. (For interpretation of the references to colour in this figure legend, the reader is referred to the web version of this article.)

grammed experiments. Along the dominant reaction pathway identified, besides the quasi-equilibrated adsorption of CH_4, it is only the dehydrogenation reaction of CH_3^* (R17) where a C—H bond cleavage is involved and no steam derived intermediates are participating.

3.7. Model parameters sensitivity

A sensitivity analysis was also conducted to identify the importance of the microkinetic model parameters. Relevant results are presented in Fig. 11, where normalised sensitivity coefficients are given for the molar fractions of CH_4, CO, CO_2 and H_2 under a perturbation of the model's parameters equal to 1%. The chemisorption heat of CH_3 is revealed to have a significant positive effect on the conversion of CH_4 and, equivalently, to the production of CO, CO_2 and H_2. Within the UBI-QEP framework an increase in the chemisorption heat of a compound leads actually to higher activation energies for steps involving the latter as a reactant. Indeed, UBI-QEP (see Eq. (7) in Supporting Information) predicts for a stronger binding of CH_3 a rise of the forward activation energy of key step R17 and a drop in the respective activation energy of the reverse step, both proportional to the perturbation imposed during SA. This would be expected to affect negatively the conversion of CH_4, however the stronger binding of CH_3 influences also the partial surface coverage of CH_3^*, effectively increasing it. The latter also directly influences the rate of reaction R17, thus, leading to an overall enhancement of the dominant reaction pathway.

As seen in Fig. 11, the chemisorption heat of CH_2 is identified as the most sensitive among all model parameters, with the parameter having a clearly positive effect on reactants consumption and products formation. As has been discussed in literature [63], also in relation to CH_4 reforming [20,21], in dissociation reactions the stronger binding of products leads to a stabilization of the respective transition state. The latter translates in a reduction of the relevant activation barrier, as is also evidenced from and discussed above for the UBI-QEP calculated activation energies. In the case of Q_{CH2} its identified importance is clearly in line with the suggested primary kinetic relevance of reaction step R17 and is responsible for the observed CH_4 conversion enhancement. A similar positive effect is observed through the SA for the chemisorption heat of H that can be attributed to an equivalent activation barrier reduction for step R17. It would be expected that the stronger binding of H hinders H_2 desorption, however model predictions suggest that the acceleration of the rate determining step overcompensates for this.

A strong negative influence of Q_C is also identified by the SA that can be correlated to the high surface coverage of C^* predicted by the model. In Fig. 12 surface coverage predictions for the two investigated materials at the varying temperature and H_2O/C ratio are presented. Clearly the catalyst surface is predominantly occupied by C^* across the studied conditions with the rest of the species possessing much lower coverages. This can be attributed to the

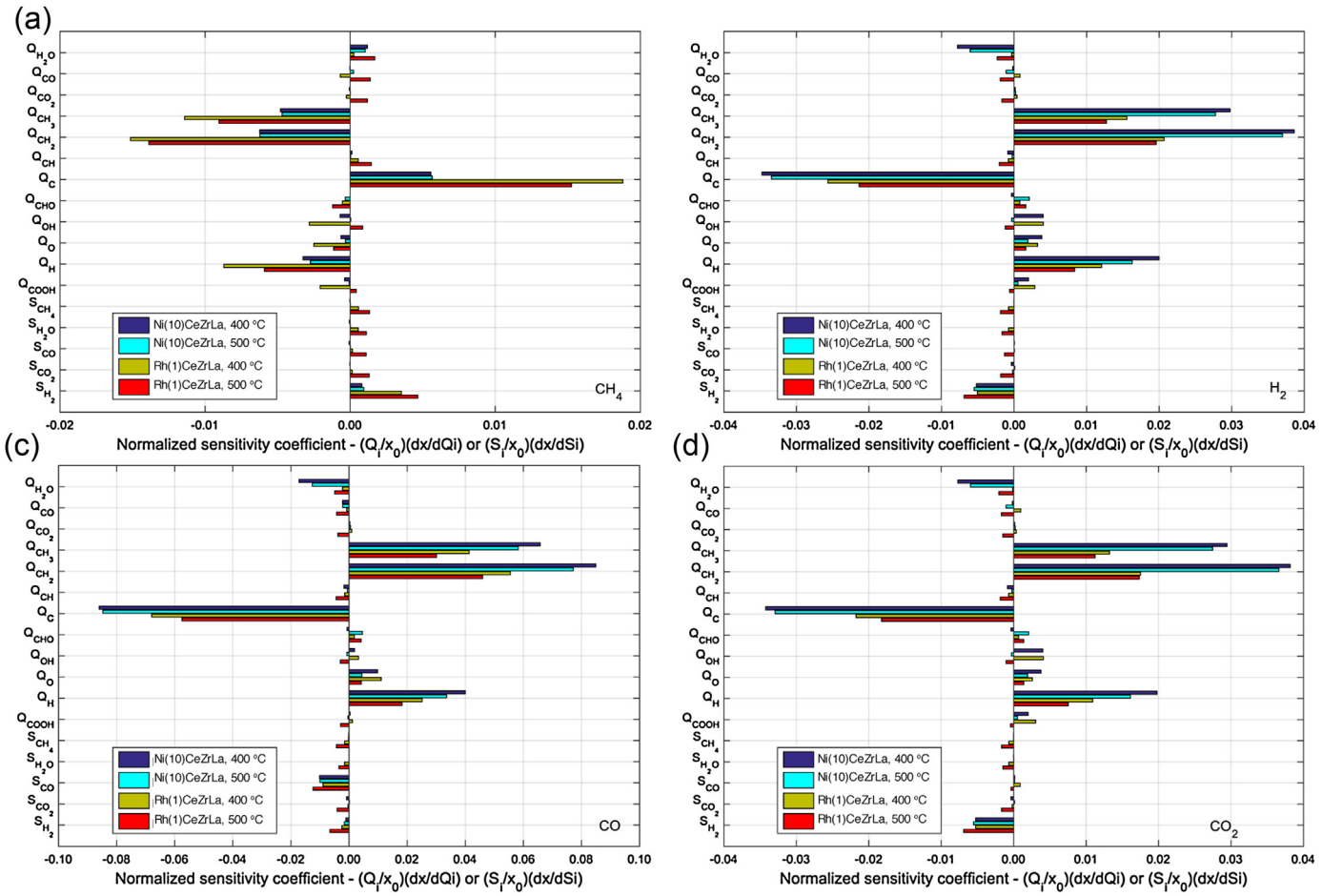

Fig. 11. Model parameters sensitivity analysis for (a) CH_4, (b) H_2, (c) CO and (d) CO_2 outlet fractions at different temperatures for Ni(10)CeZrLa and Rh(1)CeZrLa catalysts. Base values for the parameters are shown in Table 5. Operating conditions: GHSV = 7×10^4 h^{-1}, $H_2O/C = 3$.

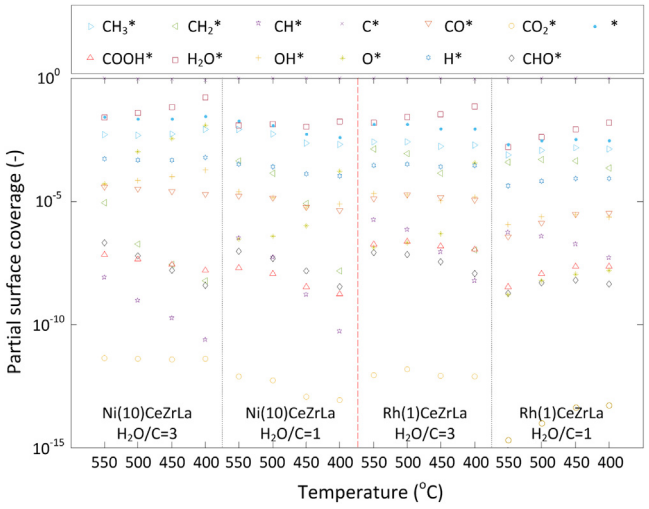

Fig. 12. Surface coverage for Ni(10)CeZrLa and Rh(1)CeZrLa catalysts at different temperatures and H_2O/C ratios. Operating conditions: GHSV = 7×10^4 h^{-1}.

strong binding of C with the catalyst surface, as indicated by the model predicted chemisorption heat Q_C that is roughly 760 kJ/mol for both materials. C* in the model is a reactive species so this effect is not associated with coke formation directly, however an even stronger binding with the surface is equivalent to an increasing difficulty to react this species off leading to a saturation of the catalyst active sites and a negative influence on reactants conversion. On the other hand, as has also been discussed in literature [20], a high surface coverage in C* is in line with progressively faster and easier H-abstractions from CH_4 to C*. This cascade process results in overall low CH_x* coverages and C* being the most abundant carbon-containing surface species as is clearly the case from Fig. 12. These carbon species on the catalyst under steam reforming conditions maintain a high, yet equilibrated, concentration, since they can be reacted off with OH* giving rise to CO*, as discussed in the reaction pathway analysis section above. The experimentally observed high resistance to coke formation, under extensive TOS tests of over 90 h under simulated biogas feed at high pressure [19], further support these findings. For the Ni(10)CeZrLa, for example, carbon deposits as low as 0.05 wt% were measured after this test, corresponding to ca. 0.01×10^{-3} % of the inlet carbon during this period. As mentioned above and as also reported elaborately in literature [64,65], a distinction needs to be made between "active" and "inactive" carbon, as the former is a reactive species participating in the reaction pathways, namely of CO production. Considering the high coverage of carbon-containing species predicted by our model and specifically of C*, it can be calculated that about 50% of the experimentally measured carbon is actually "active", suggesting that the "inactive" coke deposits are remarkably low.

It should further be noted that the OH* species responsible for carbon removal can potentially also originate from the support, if steam can be activated there, as has been observed for example on Ni/ZrO_2 [66] or $Pt/\gamma\text{-}Al_2O_3$ [67] catalysts. Similarly, lattice oxygen from the support can potentially also contribute to carbon removal

and CO oxidation [64,65,68]. The omission of support effects has, indeed, been discussed in previous studies in relation to the modelling of ethanol [69] and ethylene glycol [70] steam reforming, as a possible reason behind the reduced predictability of respective CO/CO_2 selectivities. The relatively poorer description of CO outlet concentration by our model, discussed above, could be also due to this. However, given that no KIE was observed for steam (Section 3.3), it can be assumed that these processes are not kinetically relevant at these conditions and take place faster that the activation of CH_4 via step R17. As such, the current model, even though it does not consider steam activation on the support but only on the metal, is correctly describing the experimental results. Under decomposition conditions though, as seen during the temperature programmed experiments (Section 3.2), these carbon species can only be oxidised by oxygen derived from either the surface or the bulk of the support, leading eventually to the experimentally observed performance degradation due to coke formation and oxygen depletion.

Finally, the only other model parameter that is found to have a noticeable negative sensitivity is the sticking coefficient of H_2. Unlike chemisorption heat Q_H that was found to enhance activity, this parameter, affecting the coverage of H*, but not the energetics of the kinetically relevant surface step R17, leads to a reduction of the conversion of CH_4.

3.8. Catalysts performance evaluation versus model parameters

Table 5 shows the final estimated values for the parameters of the microkinetic model presented in Table 1 together with the respective 95% confidence intervals. Following initial model development stages and after consideration of preliminary sensitivity analyses conducted (in line with Fig. 11 results) non-sensitive parameters were fixed at their estimated values to allow the refinement and more precise estimation of the more sensitive parameters. Confidence intervals shown in Table 5 are sufficiently narrow for the latter for both metals warranting low standard errors. The maximum absolute value in the correlation coefficient matrix occurs between Q_{H2O} and Q_H and is equal to −0.92 for the case of Ni. Some degree of negative correlation is hence observed between these two parameters, a fact relatively consistent with the close link of the coverages of H_2O^* and H^*. For Rh no significant correlation between the parameters of the model occurs. Values close to unity for the squared multiple correlation coefficient were obtained ($R^2_{Ni} = 0.975$ and $R^2_{Rh} = 0.954$) and high F-values (606.18 and 371.48 for Ni and Rh respectively) for the global significance of the regression (tabulated value = 3.01), ensure the model's good performance.

All estimated model parameters are within physically realistic limits and the respective values agree in general well with theoretical and experimentally reported (Table 5). As far as the most sensitive are concerned, for CH_3 typical adsorption energies for Ni(111) and Rh(111) found in literature are slightly lower (by roughly 15 kJ/mol) to the presently estimated of about 207 kJ/mol. Nonetheless, a value of 213 kJ/mol, very close to the current estimate, has been reported, based on experimentally adjusted DFT calculations, for the Ni(211) surface [36], the latter being employed to model under-coordinated step edge sites. Additionally, for Rh(111) a value of 212 kJ/mol was calculated by Walter et al. [71], again through DFT, for a partial coverage of CH_3 equal to 0.33. In the case of CH_2, again the experimentally adjusted DFT values reported by Blaylock et al. [36] (374 and 387 kJ/mol for Ni(111) and Ni(211) respectively) are in good agreement with current estimates of 372 kJ/mol for Ni(10)CeZrLa. Similar values of approximately 363 and 387 kJ/mol were calculated by Li at al. [72] over Ni(100) and Zhu at al. [73] over Ni(111), respectively, the former surface employed by the authors again to model higher reactivity sites of low coordination. CH_2 adsorption energies on Rh(111) are in general larger than those over Ni(111) where available. For example, a value of about 420 kJ/mol has been calculated in the work of Bunnik et al. [74], while an even larger adsorption energy of 457 kJ/mol was reported by Mhadeshwar et al. [28]. Current results agree qualitatively with this trend, where Q_{CH2} was estimated to be larger by 20 kJ/mol on Rh(1)CeZrLa in comparison to Ni(10)CeZrLa, although the value of about 390 kJ/mol is relatively lower to the literature ones. Nonetheless, in the work of Yang et al. [75] the reported value of 393 kJ/mol is in very good agreement with the present work. For the adsorption energy of H, a very good agreement of the estimated values of 255 kJ/mol in this work for both Ni(10)CeZrLa and Rh(1)CeZrLa can be identified with literature, where studies have typically been reporting energies ranging from 250 to 270 kJ/mol for both metals (see for example the references above). Finally, the adsorption energy of C on both catalysts at about 760 kJ/mol is slightly overestimated in comparison to reported ones, nonetheless relatively close to values obtained at specific cases, such as low coordination sites. Again on a Ni(100) surface, adsorption energies equal to 700 and 726 kJ/mol were calculated by Li at al. [72] and Blaylock et al. [36], while an experimentally reported value of 715 kJ/mol was reported by Isett et al. [76] for the same facet. On the other hand for Rh, in the work of Bunnik et al. [74] a value of 705 kJ/mol was reported for Rh(111), whereas for the same surface adsorption energies as high as 775, 813 and 825.0 kJ/mol were calculated by Zhang et al. [77], van Grootel et al. [78] and Wang et al. [79] respectively. Based on the overall satisfactory agreement described above, there is confidence that also the values of the calculated activation energies through the UBI-QEP framework lie within physically realistic limits and represent the surface energetics reasonably.

There is a trend identified in the estimated chemisorption heats, wherein most of those of CH_x^* species are larger for Rh in comparison to Ni suggesting a stronger binding for all these intermediates. This is especially true for the values of the kinetically important Q_{CH2}, which, as discussed, suggests a decrease in the energy needed for the formation of the relevant transition state of step R17. The findings of the model in this regard are in line with the overall consistent agreement in literature of the experimentally observed [20,21,80–82] and theoretically predicted [26] higher activity of Rh compared to Ni. The latter is evident in the UBI-QEP calculated activation barriers of step R17 that are lower by roughly 8 kJ/mol for Rh in comparison to Ni ($E^f_{R17-18,Rh}$ = 80.86 kJ/mol, while $E^f_{R17-18,Ni}$ = 88.23 kJ/mol). At the same time the reverse step of CH_3^* via hydrogenation of CH_2^* (R18) is also affected ($E^b_{R17-18,Rh}$ = 55.81 kJ/mol, while $E^b_{R17-18,Ni}$ = 43.57 kJ/mol), resulting in an overall considerably more endothermic reaction over Ni versus Rh ($\Delta H_{R17-18,Ni}$ = 44.66 kJ/mol, while $\Delta H_{R17-18,Rh}$ = 25.05 kJ/mol). Moreover, as has been discussed in literature e.g. for methane reforming [83] and oxidative coupling [84], such findings can facilitate catalyst design by providing guidelines for desired features. Binding energies at actual catalysts can be tuned for example by the addition of dopants, so that they are at an optimal range for achieving desired performance or even avoiding carbon deactivation [83]. Summarising, it is noted that, through the parameterisation on the basis of heats of chemisorption, the model implemented has been proven to be applicable over both Ni and Rh, successfully describing experimental data and mechanistic trends and correctly discriminating between the two metals.

4. Conclusions

In the current work a comprehensive approach was followed in order to study the kinetics of low temperature steam reforming

over nickel and rhodium catalysts supported on lanthana-doped ceria-zirconia mixed oxides. Temperature programmed experiments in combination with isotopic studies revealed that over both metals C—H bond activation is the kinetically controlling step in methane conversion, while steam was shown not to be affecting this rate. An elaborate microkinetic model was also developed to elucidate the reactants activation and conversion surface pathways. Simulation results agreed well with the experimental findings, identifying the dehydrogenation of the methyl surface species to be the rate-determining step on both metals. Moreover, model predictions were able to successfully discriminate the two metals, suggesting the higher activity of Rh over Ni on account of more stabilised key surface intermediates, in agreement with prevailing literature. The combined methodology presented in the current work shows potential as a tool to accelerate current catalyst development efforts for the low temperature steam reforming process. Further extensions are planned to explicitly account for support effects on H_2O activation, while validation over simulated biogas steam reforming experiments are planned. Ultimately, application of the model for the optimal design of a low temperature membrane steam reformer under realistic conditions is targeted.

Acknowledgements

The authors would like to acknowledge Professors Joris W. Thybaut and Guy B. Marin, Laboratory for Chemical Technology of Ghent University, for providing the Micro-Kinetic Engine (MKE) code based on which the model presented in the current work has been developed.

Appendix A. Supplementary data

Supplementary data associated with this article can be found, in the online version, at http://dx.doi.org/10.1016/j.apcatb.2016.12.033.

References

[1] J. Tong, M. Yasuyuki, Pure hydrogen production by methane steam reforming with hydrogen-permeable membrane reactor, Catal. Today 111 (2006) 147–152.
[2] S.L. Jørgensen, P.E.H. Nielsen, P. Lehrmann, Steam reforming of methane in a membrane reactor, Catal. Today 25 (1995) 303–307.
[3] J.R. Rostrup-Nielsen, J. Sehested, J.K. Norskov, Hydrogen and synthesis gas by steam- and CO_2 reforming, Adv. Catal. 47 (2002) 65–139.
[4] D.P. Ferreira-Aparicio, M.J. Benito, J.L. Sanz, New trends in reforming technologies: from hydrogen industrial plants to multifuel microreformers, Catal. Rev. 47 (2005) 491–588.
[5] S. Lee, Methane and Its Derivatives, Taylor & Francis, 1996.
[6] S.D. Angeli, G. Monteleone, A. Giaconia, A.A. Lemonidou, State-of-the-art catalysts for CH_4 steam reforming at low temperature, Int. J. Hydrogen Energy 39 (2014) 1979–1997.
[7] G. Nahar, V. Dupont, Hydrogen production from simple alkanes and oxygenated hydrocarbons over ceria–zirconia supported catalysts: review, Renew. Sustain. Energy Rev. 32 (2014) 777–796.
[8] S. Gopalakrishnan, M.G. Faga, I. Miletto, S. Coluccia, G. Caputo, S. Sau, A. Giaconia, G. Berlier, Unravelling the structure and reactivity of supported Ni particles in Ni-$CeZrO_2$ catalysts, Appl. Catal. B Environ. 138–139 (2013) 353–361.
[9] H.-S. Roh, I.-H. Eum, D.-W. Jeong, Low temperature steam reforming of methane over Ni–$Ce_{(1-x)}Zr_{(x)}O_2$ catalysts under severe conditions, Renew. Energy 42 (2012) 212–216.
[10] D.A.J.M. Ligthart, R.A. van Santen, E.J.M. Hensen, Influence of particle size on the activity and stability in steam methane reforming of supported Rh nanoparticles, J. Catal. 280 (2011) 206–220.
[11] Y. Sekine, M. Haraguchi, M. Matsukata, E. Kikuchi, Low temperature steam reforming of methane over metal catalyst supported on $Ce_xZr_{1-x}O_2$ in an electric field, Catal. Today 171 (2011) 116–125.
[12] M.H. Halabi, M.H.J.M. de Croon, J. van der Schaaf, P.D. Cobden, J.C. Schouten, Low temperature catalytic methane steam reforming over ceria–zirconia supported rhodium, Appl. Catal. A Gen. 389 (2010) 68–79.
[13] K. Kusakabe, K.-I. Sotowa, T. Eda, Y. Iwamoto, Methane steam reforming over Ce–ZrO_2-supported noble metal catalysts at low temperature, Fuel Process. Technol. 86 (2004) 319–326.
[14] J.S. Moura, J. da Silva Lima Fonseca, N. Bion, F. Epron, T. de Freitas Silva, C.G. Maciel, J.M. Assaf, M. do Carmo Rangel, Effect of lanthanum on the properties of copper, cerium and zirconium catalysts for preferential oxidation of carbon monoxide, Catal. Today 228 (2014) 40–50.
[15] D.A.J.M. Ligthart, J.A.Z. Pieterse, E.J.M. Hensen, The role of promoters for Ni catalysts in low temperature (membrane) steam methane reforming, Appl. Catal. A Gen. 405 (2011) 108–119.
[16] A.A. Lemonidou, E.C. Vagia, J.A. Lercher, Acetic acid reforming over Rh supported on La_2O_3/CeO_2–ZrO_2: catalytic performance and reaction pathway analysis, ACS Catal. 3 (2013) 1919–1928.
[17] L. Kundakovic, M. Flytzani-Stephanopoulos, Reduction characteristics of copper oxide in cerium and zirconium oxide systems, Appl. Catal. A Gen. 171 (1998) 13–29.
[18] S.D. Angeli, F.G. Pilitsis, A.A. Lemonidou, Methane steam reforming at low temperature: effect of light alkanes' presence on coke formation, Catal. Today 242 (Part A) (2015) 119–128.
[19] S.D. Angeli, L. Turchetti, G. Monteleone, A.A. Lemonidou, Catalyst development for steam reforming of methane and model biogas at low temperature, Appl. Catal. B Environ. 181 (2016) 34–46.
[20] J. Wei, E. Iglesia, Isotopic and kinetic assessment of the mechanism of reactions of CH_4 with CO_2 or H_2O to form synthesis gas and carbon on nickel catalysts, J. Catal. 224 (2004) 370–383.
[21] J. Wei, E. Iglesia, Structural requirements and reaction pathways in methane activation and chemical conversion catalyzed by rhodium, J. Catal. 225 (2004) 116–127.
[22] J. Wei, E. Iglesia, Structural and mechanistic requirements for methane activation and chemical conversion on supported iridium clusters, Angew. Chem. Int. Ed. 43 (2004) 3685–3688.
[23] J. Wei, E. Iglesia, Isotopic and kinetic assessment of the mechanism of methane reforming and decomposition reactions on supported iridium catalysts, Phys. Chem. Chem. Phys. 6 (2004) 3754–3759.
[24] J. Wei, E. Iglesia, Reaction pathways and site requirements for the activation and chemical conversion of methane on Ru-based catalysts, J. Phys. Chem. B 108 (2004) 7253–7262.
[25] J. Wei, E. Iglesia, Mechanism and site requirements for activation and chemical conversion of methane on supported Pt clusters and turnover rate comparisons among noble metals, J. Phys. Chem. B 108 (2004) 4094–4103.
[26] G. Jones, J.G. Jakobsen, S.S. Shim, J. Kleis, M.P. Andersson, J. Rossmeisl, F. Abild-Pedersen, T. Bligaard, S. Helveg, B. Hinnemann, J.R. Rostrup-Nielsen, I. Chorkendorff, J. Sehested, J.K. Nørskov, First principles calculations and experimental insight into methane steam reforming over transition metal catalysts, J. Catal. 259 (2008) 147–160.
[27] M. Maestri, D.G. Vlachos, A. Beretta, G. Groppi, E. Tronconi, A C1 microkinetic model for methane conversion to syngas on Rh/Al_2O_3, AIChE J. 55 (2009) 993–1008.
[28] A.B. Mhadeshwar, D.G. Vlachos, Hierarchical multiscale mechanism development for methane partial oxidation and reforming and for thermal decomposition of oxygenates on Rh, J. Phys. Chem. B 109 (2005) 16819–16835.
[29] M. Maestri, D.G. Vlachos, A. Beretta, G. Groppi, E. Tronconi, Steam and dry reforming of methane on Rh: microkinetic analysis and hierarchy of kinetic models, J. Catal. 259 (2008) 211–222.
[30] A. Donazzi, M. Maestri, B.C. Michael, A. Beretta, P. Forzatti, G. Groppi, E. Tronconi, L.D. Schmidt, D.G. Vlachos, Microkinetic modeling of spatially resolved autothermal CH_4 catalytic partial oxidation experiments over Rh-coated foams, J. Catal. 275 (2010) 270–279.
[31] L. Maier, B. Schädel, K. Herrera Delgado, S. Tischer, O. Deutschmann, Steam reforming of methane over nickel: development of a multi-step surface reaction mechanism, Top. Catal. 54 (2011) 845–858.
[32] K. Delgado, L. Maier, S. Tischer, A. Zellner, H. Stotz, O. Deutschmann, Surface reaction kinetics of steam- and CO2-Reforming as well as oxidation of methane over nickel-Based catalysts, Catalysts 5 (2015) 871–904.
[33] D. Chen, R. Lødeng, A. Anundskås, O. Olsvik, A. Holmen, Deactivation during carbon dioxide reforming of methane over Ni catalyst: microkinetic analysis, Chem. Eng. Sci. 56 (2001) 1371–1379.
[34] D. Chen, R. Lødeng, H. Svendsen, A. Holmen, Hierarchical multiscale modeling of methane steam reforming reactions, Ind. Eng. Chem. Res. 50 (2011) 2600–2612.
[35] D.W. Blaylock, T. Ogura, W.H. Green, G.J.O. Beran, Computational investigation of thermochemistry and kinetics of steam methane reforming on Ni(111) under realistic conditions, J. Phys. Chem. C 113 (2009) 4898–4908.
[36] D.W. Blaylock, Y.-A. Zhu, W.H. Green, Computational investigation of the thermochemistry and kinetics of steam methane reforming over a multi-faceted nickel catalyst, Top. Catal. 54 (2011) 828–844.
[37] C. Fan, Y.-A. Zhu, M.-L. Yang, Z.-J. Sui, X.-G. Zhou, D. Chen, Density functional theory-assisted microkinetic analysis of methane dry reforming on Ni catalyst, Ind. Eng. Chem. Res. 54 (2015) 5901–5913.
[38] M.A. Vannice, Kinetics of Catalytic Reactions, Springer, New York, 2005.
[39] P.B. Weisz, C.D. Prater, Interpretation of measurements in experimental catalysis, Adv. Catal. 6 (1954) 143–196.
[40] K. Metaxas, J. Thybaut, G. Morra, D. Farrusseng, C. Mirodatos, G. Marin, A microkinetic vision on high-Throughput catalyst formulation and optimization: development of an appropriate software tool, Top. Catal. 53 (2010) 64–76.
[41] C. Sprung, P.N. Kechagiopoulos, J.W. Thybaut, B. Arstad, U. Olsbye, G.B. Marin, Microkinetic evaluation of normal and inverse kinetic isotope effects during

methane steam reforming to synthesis gas over a $Ni/NiAl_2O_4$ model catalyst, Appl. Catal. A Gen. 492 (2015) 231–242.
[42] P.N. Brown, A.C. Hindmarsh, L.R. Petzold, Using Krylov methods in the solution of large-scale differential-algebraic systems, SIAM J. Sci. Comput. 15 (1994) 1467–1488.
[43] Netlib. http://www.netlib.org/, (n.d.).
[44] H.H. Rosenbrock, An automatic method for finding the greatest or least value of a function, Comput. J. 3 (1960) 175–184.
[45] D.W. Marquardt, An algorithm for least-squares estimation of nonlinear parameters, J. Soc. Ind. Appl. Math. 11 (1963) 431–441.
[46] P.T. Boggs, J.R. Donaldson, R. h. Byrd, R.B. Schnabel, Algorithm 676: ODRPACK: software for weighted orthogonal distance regression, ACM Trans. Math. Softw. 15 (1989) 348–364.
[47] J.M. Caruthers, J.A. Lauterbach, K.T. Thomson, V. Venkatasubramanian, C.M. Snively, A. Bhan, S. Katare, G. Oskarsdottir, Catalyst design: knowledge extraction from high-throughput experimentation, J. Catal. 216 (2003) 98–109.
[48] E. Shustorovich, The bond-order conservation approach to chemisorption and heterogeneous catalysis: applications and implications, Adv. Catal. 37 (1990) 101–163.
[49] E. Shustorovich, H. Sellers, The UBI-QEP method: a practical theoretical approach to understanding chemistry on transition metal surfaces, Surf. Sci. Rep. 31 (1998) 1–119.
[50] B.C. Enger, R. Lødeng, A. Holmen, On the nature of elementary reactions from methane to hydrogen over transition metals, Int. J. Hydrogen Energy 37 (2012) 10418–10424.
[51] N. Laosiripojana, S. Assabumrungrat, Methane steam reforming over $Ni/Ce-ZrO_2$ catalyst: influences of $Ce-ZrO_2$ support on reactivity, resistance toward carbon formation, and intrinsic reaction kinetics, Appl. Catal. A Gen. 290 (2005) 200–211.
[52] T.-J. Huang, C.-H. Wang, Roles of surface and bulk lattice oxygen in forming CO_2 and CO during methane reaction over gadolinia-doped ceria, Catal. Lett. 118 (2007) 103–108.
[53] M.H. Halabi, M.H.J.M. De Croon, J. Van Der Schaaf, P.D. Cobden, J.C. Schouten, Intrinsic kinetics of low temperature catalytic methane-steam reforming and water-gas shift over $Rh/Ce_\alpha Zr_{1-\alpha}O_2$ catalyst, Appl. Catal. A Gen. 389 (2010) 80–91.
[54] S. Yokota, K. Okumura, M. Niwa, Support effect of metal oxide on Rh catalysts in the CH_4 - CO_2 reforming reaction, Catal. Lett. 84 (2002) 131–134.
[55] R. Wang, H. Xu, X. Liu, Q. Ge, W. Li, Role of redox couples of $Rh0/Rh^{\delta+}$ and Ce^{4+}/Ce^{3+} in CH_4/CO_2 reforming over $Rh-CeO_2/Al_2O_3$ catalyst, Appl. Catal. A Gen. 305 (2006) 204–210.
[56] J. Carrasco, L. Barrio, P. Liu, J.A. Rodriguez, M.V. Ganduglia-Pirovano, Theoretical studies of the adsorption of CO and C on Ni(111) and $Ni/CeO_2(111)$: Evidence of a strong metal-support interaction, J. Phys. Chem. C 117 (2013) 8241–8250.
[57] M. Gómez-Gallego, M.A. Sierra, Kinetic isotope effects in the study of organometallic reaction mechanisms, Chem. Rev. (Washington DC, United States) 111 (2011) 4857–4963.
[58] A. Ozaki, Isotopic Studies of Heterogenous Catalysis, Kodansha Ltd & Academic Press Inc., Tokyo-London, 1977.
[59] C. Sprung, B. Arstad, U. Olsbye, Methane steam reforming over a $Ni/NiAl_2O_4$ model catalyst-kinetics, ChemCatChem 6 (2014) 1969–1982.
[60] T. Osaki, T. Horiuchi, K. Suzuki, T. Mori, CH_4/CD_4 isotope effect on the reaction of adsorbed hydrocarbon species in CO_2-reforming over Ni/Al_2O_3 catalyst, Catal Lett. 44 (1997) 19–21.
[61] K. Otsuka, S. Kobayashi, S. Takenaka, Hydrogen–deuterium exchange studies on the decomposition of methane over Ni/SiO_2, J. Catal. 200 (2001) 4–9.
[62] L.M. Aparicio, Transient isotopic studies and microkinetic modeling of methane reforming over nickel catalysts, J. Catal. 165 (1997) 262–274.
[63] Z.-P. Liu, P. Hu, General rules for predicting where a catalytic reaction should occur on metal surfaces: a density functional theory study of C-H and C-O bond breaking/making on flat, stepped, and kinked metal surfaces, J. Am. Chem. Soc. 125 (2003) 1958–1967.
[64] M.M. Makri, M.A. Vasiliades, K.C. Petallidou, A.M. Efstathiou, Effect of support composition on the origin and reactivity of carbon formed during dry reforming of methane over 5 wt% $Ni/Ce_{1-x}M_xO_{2-\delta}$ ($M = Zr^{4+}$, Pr^{3+}) catalysts, Catal. Today 259 (2016) 150–164.
[65] M.A. Vasiliades, M.M. Makri, P. Djinović, B. Erjavec, A. Pintar, A.M. Efstathiou, Dry reforming of methane over 5 wt% $Ni/Ce_{1-x}Pr_xO_2$ catalysts: performance and characterisation of active and inactive carbon by transient isotopic techniques, Appl. Catal. B Environ. 197 (2016) 168–183.
[66] Y. Matsumura, T. Nakamori, Steam reforming of methane over nickel catalysts at low reaction temperature, Appl. Catal. A Gen. 258 (2004) 107–114.
[67] C.M. Kalamaras, G.G. Olympiou, A.M. Efstathiou, The water-gas shift reaction on $Pt/\gamma-Al_2O_3$ catalyst: operando SSITKA-DRIFTS-mass spectroscopy studies, Catal. Today 138 (2008) 228–234.
[68] T. Bunluesin, R.J. Gorte, G.W. Graham, Studies of the water-gas-shift reaction on ceria-supported Pt, Pd, and Rh: implications for oxygen-storage properties, Appl. Catal. B Environ. 15 (1998) 107–114.
[69] J.E. Sutton, P. Panagiotopoulou, X.E. Verykios, D.G. Vlachos, D.F.T. Combined, Microkinetic, and experimental study of ethanol steam reforming on Pt, J. Phys. Chem. C 117 (2013) 4691–4706.
[70] M.A. Christiansen, D.G. Vlachos, Microkinetic modeling of Pt-catalyzed ethylene glycol steam reforming, Appl. Catal. A Gen. 431 (2012) 18–24.
[71] E.J. Walter, A.M. Rappe, Coadsorption of methyl radicals and oxygen on Rh(1 1 1), Surf. Sci. 549 (2004) 265–272.
[72] J. Li, E. Croiset, L. Ricardez-Sandoval, Methane dissociation on Ni (100), Ni (111), and Ni (553): a comparative density functional theory study, J. Mol. Catal. A Chem. 365 (2012) 103–114.
[73] Y.A. Zhu, D. Chen, X.G. Zhou, W.K. Yuan, DFT studies of dry reforming of methane on Ni catalyst, Catal. Today 148 (2009) 260–267.
[74] B.S. Bunnik, G.J. Kramer, Energetics of methane dissociative adsorption on Rh{111} from DFT calculations, J. Catal. 242 (2006) 309–318.
[75] M.-M. Yang, X.-H. Bao, W.-X. Li, Density functional theory study of CH_x (x = 1–3) adsorption on clean and CO precovered Rh(111) surfaces, J. Chem. Phys. 127 (2007) 24705.
[76] L.C. Isett, J.M. Blakely, Segregation isosteres for carbon at the (100) surface of nickel, Surf. Sci. 58 (1976) 397–414.
[77] J. Zhang, X.-M. Cao, P. Hu, Z. Zhong, A. Borgna, P. Wu, Density functional theory studies of ethanol decomposition on Rh(211), J. Phys. Chem. C 115 (2011) 22429–22437.
[78] P.W. van Grootel, R.A. van Santen, E.J.M. Hensen, Methane dissociation on high and low indices Rh surfaces, J. Phys. Chem. C 115 (2011) 13027–13034.
[79] B. Wang, L. Song, R. Zhang, The dehydrogenation of CH_4 on Rh(111), Rh(110) and Rh(100) surfaces: a density functional theory study, Appl. Surf. Sci. 258 (2012) 3714–3722.
[80] J.R. Rostrup-Nielsen, Activity of nickel catalysts for steam reforming of hydrocarbons, J. Catal. 31 (1973) 173–199.
[81] J.R. Rostrup-Nielsen, J.H.B. Hansen, CO_2-Reforming of methane over transition metals, J. Catal. 144 (1993) 38–49.
[82] D. Qin, J. Lapszewicz, Study of mixed steam and CO_2 reforming of CH_4 to syngas on MgO-supported metals, Catal. Today 21 (1994) 551–560.
[83] D. Chen, E. Bjørgum, R. Lødeng, K. Omdahl Christensen, A. Holmen, Microkinetic model assisted catalyst design for steam methane reforming, Stud. Surf. Sci. Catal. 147 (2004) 139–144.
[84] P.N. Kechagiopoulos, L. Olivier, C. Daniel, A.C. van Veen, J. Thybaut, G. Marin, C. Mirodatos, Combining catalyst formulation and microkinetic methodologies in the detailed understanding and optimization of methane oxidative coupling, in: Small-Scale Gas to Liq Fuel Synth., CRC Press, 2015, pp. 227–261.